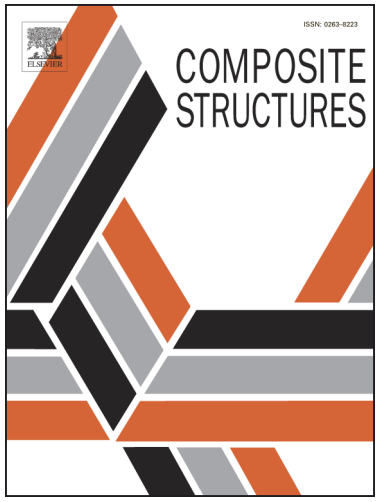

Elastic and Transport Properties of the Tailorable Multifunctional Hierarchical Honeycombs

Yongtao Sun, Qiang Chen, Nicola Pugno

PII: S0263-8223(13)00335-8
DOI: http://dx.doi.org/10.1016/j.compstruct.2013.07.012
Reference: COST 5245

To appear in: *Composite Structures*

Please cite this article as: Sun, Y., Chen, Q., Pugno, N., Elastic and Transport Properties of the Tailorable Multifunctional Hierarchical Honeycombs, *Composite Structures* (2013), doi: http://dx.doi.org/10.1016/j.compstruct.2013.07.012

Elastic and Transport Properties of the Tailorable Multifunctional Hierarchical Honeycombs

Yongtao Sun[1], Qiang Chen[2], Nicola Pugno[3*]

[1]*Laboratory of Bio-Inspired Nanomechanics "Giuseppe Maria Pugno", Department of Structural, Geotechnical and Building Engineering, Politecnico di Torino, Corso Duca degli Abruzzi 24, Torino 10129, Italy*

[2]*Laboratory of Biomechanics, School of Biological Science and Medical Engineering, Southeast University, Nanjing 210096, PR China*

[3]*Laboratory of Bio-Inspired & Graphene Nanomechanics, Departmentof Civil, Environmental and Mechanical Engineering, University of Trento, via Mesiano 77, Trento I-38123, Italy*

**Corresponding author: nicola.pugno@unitn.it*

Tel.:+39-0461-282525; Fax: +39-0461-282599.

Revised paper(unmarked), submitted to Composite Structures

Abstract

Compared with triangular, square and Kagome honeycombs, hexagonal honeycombs have lower in-plane stiffness, which restricts their multifunctional applications. Focusing on this problem, in this paper, we analytically study the in-plane elastic and transport properties of a kind of hexagonal honeycombs, i.e., the multifunctional hierarchical honeycomb (MHH). The MHH structure is developed by replacing the solid cell walls of the original regular hexagonal honeycomb (ORHH) with three kinds of equal mass isotropic honeycomb sub-structures possessing hexagonal, triangular and Kagome lattices. Formulas to derive the effective in-plane elastic properties of the regular hexagonal honeycombs at all densities are developed for analyzing the MHH structure. Results show that the hexagonal sub-structure does not improve much the elastic properties of the MHH structure. However, the triangular and Kagome sub-structures result in a substantial improvement by 1 magnitude or even 3 orders of magnitude on the Young's and shear moduli of the MHH structure, depending on the cell-wall thickness-to-length ratio of the ORHH. Besides, the effective in-plane conductivities (or dielectric constants) of the three different MHH structures are also studied. The presented theory could be used in designing new tailorable hierarchical honeycomb structures for multifunctional applications.

Keywords: In-plane effective moduli; In-plane effective conductivity (or dielectric constants); Original regular hexagonal honeycomb (ORHH); Multifunctional hierarchical honeycomb (MHH).

1. Introduction

Low-density cellular materials widely exist in nature and exhibit fascinating mechanical properties in the aspects of strength, stiffness, toughness, etc. [1-3]. As one kind of typical low density cellular solids, honeycombs, which are mainly used as cores of the light-weight sandwich panel structures [4-7], have been used in many diverse fields, such as aerospace and automotive industries. Apart from their peculiar low-density and mechanical properties, honeycombs also show other attractive functionalities, e.g., heat transfer, thermal protection, catalysis application and so on. In order to find optimal topologies for different multifunctional applications, varieties of prismatic honeycombs have been studied in recent years.

Regarding the multifunctionality of honeycomb materials , Lu [8] and Gu et al. [9] reported that regular hexagonal metal cells, comparing with triangular and square cells, provide the highest level of heat dissipation, as comparable to that of the open-cell metal foams. Combining the experimental and numerical methods, Wen et al. [10] revealed that the overall thermal performance of metal honeycomb structures are superior to other heat sink media, such as metal foams, lattice-frame materials, 3D Kagome structures and woven textile structures. Employing the topology optimization technique, Hyun and Torquato [11] showed that the effective conductivity of the regular hexagonal honeycomb is nearly approaching the Hashin-Shtrikman (H-S) upper bounds; while for triangular and Kagome honeycombs, both the in-plane effective moduli and conductivity are approaching the H-S upper bounds [12-13]. Besides, Evans et al. [14], Wadley et al. [15] and Wadley [16] reviewed the multifunctionalities and the fabrication technologies of the multifunctional periodic cellular metals with different topological structures. Hayes et al. [17] studied the mechanical and thermal properties of linear cellular alloys with square cells, and concluded that the mechanical and heat transfer characteristics of the honeycomb materials outperformed those of the open- and closed-cell metal foams with comparable relative density. Vaziri and collaborators focused on metallic sandwich panels with different kinds of cellular cores

such as hexagonal honeycombs [18], square honeycombs [19-23], open-cell rhombic dodecahedron cellular structures [24] and pyramidal truss cores [25-28], and explored some of their multifunctional applications, such as energy absorptions [27], sustaining shock loadings [19-21] and underwater impulsive loadings [22-23].

Regarding the mechanical properties of honeycomb materials, Wang and McDowell [29] investigated the in-plane stiffness and yield strength of different periodic metal honeycombs, and showed that the diamond, triangular and Kagome cells have superior in-plane mechanical properties to the hexagonal, rectangular and mixed square/triangular cells. Fleck and Qiu [30] analyzed the damage tolerance property of 2D elastic-brittle isotropic honeycombs and reported that Kagome cells have much higher fracture toughness than those of the hexagonal and triangular cells.

Another character related to honeycomb materials is the concept of hierarchy. Compared with their single length scale microstructure counterparts, structural hierarchy in natural materials can result in significantly higher stiffness or strength efficiencies (i.e. stiffness- or strength-to-weight ratios), and at the same time maintain their flaw-tolerance or energy-absorbing property [31-36]. Combining the low-weight property of cellular solids and the particular functions that natural hierarchical materials display, many researchers [37-44] have focused on the mechanical properties of the hierarchical cellular structures. Burgueno et al. [45] studied the hierarchical cellular designs for load-bearing bio-composite beams and plates. Kooistra et al. [46] investigated hierarchical corrugated core sandwich panels and revealed that second-order trusses could have much higher compressive and shear strengths than their equal-mass first-order counterparts when the relative densities are less than 5%. Fan et al. [47] studied two-dimensional cellular materials made up of sandwich struts and showed that the relevant mechanical properties of the materials were improved substantially by incorporating structural hierarchy. Inspired by diatom algae which contains nanoporous hierarchical silicified shells, Garcia et al. [48] revealed the toughening mechanism in the superductile wavy silica nanostructures by performing a series of molecular dynamics simulations. Taylor et al. [49] introduced the functionally graded hierarchical honeycombs by

performing a set of finite element analyses, and their results suggested that the elastic modulus of the functionally graded hierarchical honeycomb could be 1.75 times that of its equal-mass first-order hexagonal honeycomb if the structure is designed properly. Different from the topology of the common hierarchical honeycomb structures [37-38, 43, 49], Vaziri's group recently [50] developed a new hierarchical honeycomb structure by replacing every three-edge joint of a regular hexagonal lattice with a smaller hexagon, and showed that the elastic moduli of the hierarchical honeycombs with one level and two levels can be 2.0 and 3.5 times stiffer than their equal-mass regular hexagonal honeycomb, respectively. And more, inspired by natural materials, Chen and Pugno [42-44] explored nanomechanics of 2D hierarchical honeycombs and 3D hierarchical foams.

In this paper, following the above works, we analytically study the in-plane elastic moduli and thermal conductivity of the multifunctional hierarchical honeycomb (MHH). The term "multifunctional" is here used to describe a material that has different peculiar functions activated simultaneously by the same concept of "hierarchy". The MHH structure is formed by replacing the solid cell walls of an original regular hexagonal honeycomb (ORHH) with three different isotropic honeycomb sub-structures possessing hexagonal, triangular or Kagome lattices. First, we derive the analytical formulas of the effective elastic moduli of the regular hexagonal honeycombs for all densities. Then, the in-plane Young's, shear and bulk moduli of the three kinds of MHH structures are calculated. Besides, the effective in-plane conductivities of the three kinds of MHH structures are formulated through the H-S upper bounds.

2. Effective in-plane elastic moduli of the regular hexagonal honeycombs for all densities

Hyun and Torquato [51] analytically studied the effective in-plane properties of the regular hexagonal honeycomb for all densities via the three-point approximations and expressed the effective Young's modulus E_e (Fig. 1b) as

$$\frac{E_e}{E_s}=\frac{\phi(2\zeta-1)(\zeta+\eta-1)}{\left\{3-2\phi-2(2-\phi)(1-\zeta)+(2-\zeta-\eta)\left[2\phi(1-\zeta)-1\right]\right\}} \tag{1}$$

in which ϕ is the relative density of the hexagonal honeycomb, E_s is the Young's modulus of the constituent solid, ζ and η are the three-point parameters (Fig. 1a). The simulation data of the effective Young's modulus E_e [51] are also provided in Fig. 1b. It is apparent that for the high density case ($\phi \geq 0.5$), the three-point approximations method matches very well the simulation data, but for the lower densities it overestimates the results. In the very low density case, the overestimation is so large that the three-point approximations method is not suitable.

It is well-known that for the low-density regular hexagonal honeycombs, the Euler beam theory and the Timoshenko beam theory could be used to obtain very good analytical results for predicting their elastic parameters. Here, in order to get the analytical formulas for the in-plane elastic parameters of the regular hexagonal honeycomb at all densities, we apply the Euler beam theory and the Timoshenko beam theory to the entire range of the relative density and compare the results with the three-point approximations. Under the Euler beam theory, Torquato et al. [52] expressed the effective Young's modulus E_e as:

$$\frac{E_e}{E_s} = \frac{3}{2}\phi^3 \tag{2}$$

On the other hand, Gibson and Ashby [3] studied the elastic properties of the low density honeycombs using the Timoshenko beam theory. For the regular hexagonal honeycombs, the effective Young's modulus is given by:

$$\frac{E_e}{E_s} = \frac{4}{\sqrt{3}}\left(\frac{t}{l}\right)^3 \frac{1}{1+\left(5.4+1.5\nu_s\right)\left(t/l\right)^2} \tag{3}$$

in which ν_s is the Poisson's ratio of the constituent solid and $t/l = \sqrt{3}\left(1-\sqrt{1-\phi}\right)$ is the cell wall thickness-to-length ratio.

For honeycombs at all densities, the comparisons between the Euler beam theory, Timoshenko beam theory, three-point approximations method and the simulation data are plotted in Fig.1b. We can see that when $\phi \leq 0.5$ the results calculated by the Euler beam theory matches very well the

simulation data, while the results are well predicted by the three-point approximations when $\phi > 0.5$. Therefore, the effective Young's modulus of the regular hexagonal honeycombs for all densities can be expressed as:

$$\frac{E_e}{E_s} = \begin{cases} \frac{3}{2}\phi^3 & \phi \le 0.5 \\ \frac{\phi(2\zeta-1)(\zeta+\eta-1)}{\{3-2\phi-2(2-\phi)(1-\zeta)+(2-\zeta-\eta)[2\phi(1-\zeta)-1]\}} & \phi > 0.5 \end{cases} \tag{4}$$

Besides, through the three-point approximations, Hyun and Torquato [51] also developed the expression for the effective in-plane bulk modulus k_e of the regular hexagonal honeycombs at all densities:

$$\frac{k_e}{k_s} = \frac{G_s\phi(2\zeta-1)}{k_s(1-\phi)+G_s[1+2\phi(\zeta-1)]} = \frac{G_s/k_s\,\phi(2\zeta-1)}{(1-\phi)+G_s/k_s[1+2\phi(\zeta-1)]} \tag{5}$$

where k_s and G_s are the bulk and shear moduli of the constituent solid, respectively.

Because of the in-plane isotropic properties, k_s and E_s, k_e, G_e and E_e satisfy the following relationships:

$$k_s = \frac{E_s}{2(1-\nu_s)} \tag{6}$$

$$k_e = \frac{E_e}{2(1-\nu_e)} \tag{7}$$

$$G_e = \frac{E_e}{2(1+\nu_e)} \tag{8}$$

in which G_e and ν_e are the effective in-plane shear modulus and Poisson's ratio of the hexagonal honeycombs, respectively. Defining $E_e/E_s = A$ and $k_e/k_s = B$, Eqs. (4-8) provide the formula for G_e:

$$\frac{G_e}{E_s} = \frac{AB}{4B-2A(1-\nu_s)} \tag{9}$$

Then, the effective Poisson's ratio ν_e of the regular hexagonal honeycombs can be derived through

dividing Eq. (6) by Eq. (7):

$$\nu_e = 1 - \frac{A}{B}(1-\nu_s) \tag{10}$$

To verify the expressions of E_e, k_e and G_e, Eq. (10) is depicted in Fig. 2 for the honeycombs at all densities with $\nu_s = 1/3$. Note that in the calculations, the three-point parameters ζ and η are interpolated from Fig.1a and the relation $G_s = E_s/\left[2(1+\nu_s)\right]$ is used.

Fig. 2 shows excellent agreement with the existing results [3, 53], that is to say, the 2D effective Poisson's ratio flows to a fixed point as the percolation threshold is reached. Here ν_e tends to 1 for the extreme low densities and tends to the Poisson's ratio of constituent solid $\nu_s = 1/3$ for the extreme high densities. This implies the validations of Eqs. (4), (5) and (9). It is worth to point out that different from the formula in Ref. [3], here the Poisson's ratio is not a constant when the relative density is low.

3. MHH with isotropic hexagonal sub-structure

3.1 Basic theory

First of all, we consider the MHH with isotropic hexagonal lattice sub-structure (Fig. 3). Fig. 3a is an ORHH with the cell-wall thickness and length denoted by t_0 and l_0, respectively; Fig. 3b is an equal-mass MHH with the cell-wall thickness and length denoted by t_1 and l_0, respectively. We can see that the cell-wall lengths of the ORHH and the MHH are identical. In particular, one of the MHH cell walls in Fig. 3b is shown in Fig. 3c, and the cell-wall thickness and length for hexagonal cells are denoted by t_h and l_h, respectively. The out-of-plane depth is a constant and identical for both structures.

The geometry of Fig. 3c implies:

$$l_0 = nl_h + (n+1)(2l_h) = (3n+2)l_h \tag{11}$$

where, n is the number of the solid hexagonal cell walls lying on the middle line of the MHH cell

walls (e.g., in Fig. 3c, *n*=8). Defining $\lambda = l_h / l_0$ as the hierarchical length ratio, rearranging Eq. (11) provides,

$$\lambda = \frac{1}{3n+2} \tag{12}$$

Then, defining *N* as the number of hexagonal cells away from the middle line of the MHH cell walls (e.g., in Fig. 3c, *N*=1), and *M* the total number of half-thickness hexagonal cells in a MHH cell wall (see Fig. A in appendix A), the relationship between *M* and *N* can be expressed as:

$$M = 2N(2n+1) + \frac{n}{3} - 4A_N \tag{13}$$

with $A_N = \left[(2N+1)(N-1)+1\right]/6$ (see Appendix A). After that, basing on the mass equivalence between cell walls of the MHH and the ORHH, we find $t_0 l_0 - \frac{1}{2\sqrt{3}} t_0^2 = 6 \times \frac{1}{2}\left(t_h l_h - \frac{1}{2\sqrt{3}} t_h^2 \right) M$, which gives

$$\frac{t_h}{l_h} = \sqrt{3}\left[1 - \sqrt{1 - \frac{2}{3\sqrt{3}\lambda^2 M} \frac{t_0}{l_0}\left(1 - \frac{1}{2\sqrt{3}} \frac{t_0}{l_0} \right)} \right] \tag{14}$$

Besides, a geometrical analysis on Fig. 3c provides $N_{\max}$, the upper bound of N, and t_1, the thickness of the MHH cell walls：

$$N_{\max} = fl\left[\frac{1}{2\lambda} \right] = fl\left[\frac{3n+2}{2} \right] \tag{15}$$

$$t_1 = \begin{cases} 2N\left(\sqrt{3} l_h\right) + t_h & 1 \le N \le N_{\max} - 1 \\ 2 \times \frac{\sqrt{3}}{2} l_0 & N = N_{\max} \end{cases} \tag{16}$$

where, '*fl*[ ]' is the floor function, which denotes the largest integer not greater than the term in the bracket. Then, rearranging Eq. (16) gives:

$$\frac{t_1}{l_0} = \begin{cases} \left(2\sqrt{3}N + \frac{t_h}{l_h} \right)\lambda & 1 \le N \le N_{\max} - 1 \\ \sqrt{3} & N = N_{\max} \end{cases} \tag{17}$$

On the other hand, with respect to Eq. (14), the relation $1-2\Big/\left(3\sqrt{3}\lambda^2 M\right)t_0/l_0\left[1-1\Big/\left(2\sqrt{3}\right)t_0/l_0\right]\geq 0$ should be satisfied. Considering Eqs. (12) and (13), this relation provides $N_{\min}$, the lower bound of N:

$$N_{\min}=ce\left[\frac{3n+2-\sqrt{(3n+2)^2\left[1-\frac{2}{\sqrt{3}}\frac{t_0}{l_0}\left(1-\frac{1}{2\sqrt{3}}\frac{t_0}{l_0}\right)\right]+n}}{2}\right] \tag{18}$$

where, '*ce*[ ]' is the ceiling function, which denotes the smallest integer not less than the term in the bracket. Note that Eq. (18) may give $N_{\min}=0$, in this case $N_{\min}=1$.

Defining the in-plane Young's, shear and bulk moduli of the ORHH as E_O, G_O and k_O, then, from Eqs. (4), (5) and (9), we find:

$$\frac{E_O}{E_s}=A_O=\begin{cases}\dfrac{3}{2}\phi_O^3 & \phi_O\leq 0.5\\ \dfrac{\phi_O\left(2\zeta_O-1\right)\left(\zeta_O+\eta_O-1\right)}{\left\{3-2\phi_O-2\left(2-\phi_O\right)\left(1-\zeta_O\right)+\left(2-\zeta_O-\eta_O\right)\left[2\phi_O\left(1-\zeta_O\right)-1\right]\right\}} & \phi_O>0.5\end{cases} \tag{19}$$

$$\frac{k_O}{k_s}=B_O=\frac{G_s/k_s\,\phi_O\left(2\zeta_O-1\right)}{\left(1-\phi_O\right)+G_s/k_s\left[1+2\phi_O\left(\zeta_O-1\right)\right]} \tag{20}$$

$$\frac{G_O}{E_s}=\frac{A_O B_O}{4B_O-2A_O\left(1-\nu_s\right)} \tag{21}$$

where,

$$\phi_O=\frac{2}{\sqrt{3}}\frac{t_0}{l_0}-\frac{1}{3}\left(\frac{t_0}{l_0}\right)^2\quad\left(\frac{t_0}{l_0}\leq\sqrt{3}\right) \tag{22}$$

is the relative density of the ORHH, and ζ_O and η_O, interpolated from Fig. 1a, are the corresponding three-point parameters.

Besides, Hyun and Torquato [11, 51] showed that the effective thermal conductivity of the regular hexagonal honeycomb nearly approaches the H-S upper bounds. Thus, defining the thermal

conductivities of the ORHH and the constituent solid as σ_O and σ_s, we approximately obtain:

$$\frac{\sigma_O}{\sigma_s}=\frac{\phi_O}{2-\phi_O} \tag{23}$$

Note that due to the mathematical analogy, results for the effective thermal conductivity translate immediately into the equivalent results for the effective dielectric constant, electrical conductivity and magnetic permeability.

Similarly, defining the in-plane Young's, shear and bulk moduli and thermal conductivity of the hexagonal sub-structure as E_h, G_h, k_h and σ_h, we obtain:

$$\frac{E_h}{E_s}=A_h=\begin{cases}\dfrac{3}{2}\phi_h^3 & \phi_h\le 0.5\\ \dfrac{\phi_h\left(2\zeta_h-1\right)\left(\zeta_h+\eta_h-1\right)}{\left\{3-2\phi_h-2\left(2-\phi_h\right)\left(1-\zeta_h\right)+\left(2-\zeta_h-\eta_h\right)\left[2\phi_h\left(1-\zeta_h\right)-1\right]\right\}} & \phi_h>0.5\end{cases} \tag{24}$$

$$\frac{k_h}{k_s}=B_h=\frac{G_s/k_s\,\phi_h\left(2\zeta_h-1\right)}{\left(1-\phi_h\right)+G_s/k_s\left[1+2\phi_h(\zeta_h-1)\right]} \tag{25}$$

$$\frac{G_h}{E_s}=\frac{A_hB_h}{4B_h-2A_h\left(1-\nu_s\right)} \tag{26}$$

$$\frac{\sigma_h}{\sigma_s}=\frac{\phi_h}{2-\phi_h} \tag{27}$$

where,

$$\phi_h=\frac{2}{\sqrt{3}}\frac{t_h}{l_h}-\frac{1}{3}\left(\frac{t_h}{l_h}\right)^2\quad\left(\frac{t_h}{l_h}\le\sqrt{3}\right) \tag{28}$$

is the relative density of the hexagonal sub-structure, and ζ_h and η_h, interpolated from Fig. 1a, are the corresponding three-point parameters. Denoting the effective Poisson's ratio of the hexagonal sub-structure by ν_h, the relation $G_h=E_h/\left[2(1+\nu_h)\right]$ is satisfied. Then, combining Eqs. (24) and (26) gives,

$$\nu_h=1-\frac{A_h}{B_h}(1-\nu_s) \tag{29}$$

Thus,

$$\frac{G_h}{k_h}=\frac{E_h/\left[2(1+\nu_h)\right]}{E_h/\left[2(1-\nu_h)\right]}=\frac{1-\nu_h}{1+\nu_h}=\frac{A_h(1-\nu_s)}{2B_h-A_h(1-\nu_s)} \tag{30}$$

At the same time, by treating the hexagonal sub-structure as a continuum and defining the in-plane Young's, shear and bulk moduli and thermal conductivity of the MHH as E_M, G_M, k_M and σ_M, it is easy to obtain:

$$\frac{E_M}{E_h}=A_M=\begin{cases}\dfrac{3}{2}\phi_M^3 & \phi_M\le 0.5\\ \dfrac{\phi_M(2\zeta_M-1)(\zeta_M+\eta_M-1)}{\left\{3-2\phi_M-2(2-\phi_M)(1-\zeta_M)+(2-\zeta_M-\eta_M)\left[2\phi_M(1-\zeta_M)-1\right]\right\}} & \phi_M>0.5\end{cases} \tag{31}$$

$$\frac{k_M}{k_h}=B_M=\frac{G_h/k_h\,\phi_M(2\zeta_M-1)}{(1-\phi_M)+G_h/k_h\left[1+2\phi_M(\zeta_M-1)\right]} \tag{32}$$

$$\frac{G_M}{E_h}=\frac{A_M B_M}{4B_M-2A_M(1-\nu_h)} \tag{33}$$

$$\frac{\sigma_M}{\sigma_h}=\frac{\phi_M}{2-\phi_M} \tag{34}$$

where,

$$\phi_M=\frac{2}{\sqrt{3}}\frac{t_1}{l_0}-\frac{1}{3}\left(\frac{t_1}{l_0}\right)^2\left(\frac{t_1}{l_0}\le\sqrt{3}\right) \tag{35}$$

and ζ_M and η_M, interpolated from Fig. 1a, are the three-point parameters corresponding to ϕ_M.

Combining Eqs. (19), (24) and (31) gives the relative Young's modulus E_M/E_O:

$$\frac{E_M}{E_O}=\frac{A_M A_h}{A_O} \tag{36}$$

Similarly, from Eqs. (20), (25) and (32), we can get the relative in-plane bulk modulus k_M/k_O:

$$\frac{k_M}{k_O}=\frac{B_M B_h}{B_O} \tag{37}$$

And from Eqs. (21), (24) and (33), we obtain the relative shear modulus G_M/G_O:

$$\frac{G_M}{G_O}=\frac{A_M B_M A_h}{2B_M-A_M(1-\nu_h)}\frac{2B_O-A_O(1-\nu_s)}{A_O B_O} \tag{38}$$

Finally, from Eqs. (23), (27) and (34), we get the relative thermal conductivity σ_M/σ_O:

$$\frac{\sigma_M}{\sigma_O}=\frac{\phi_M\phi_h(2-\phi_O)}{\phi_O(2-\phi_M)(2-\phi_h)} \tag{39}$$

3.2 Effect of N on the relative elastic moduli and thermal conductivity of the MHH with hexagonal sub-structure

To investigate the influence of N on the relative elastic parameters E_M/E_O, G_M/G_O, k_M/k_O and the relative thermal conductivity σ_M/σ_O, here, we discuss the following examples with parameters $n=16$, $\lambda=1/(3n+2)=0.02$ and $t_0/l_0=0.01$, 0.05, 0.1, 0.2 and 0.3. Then, we can find $N_{\max}=25$ through Eq. (15), and $N_{\min}$ for each t_0/l_0 through Eq. (18). The results of the relative elastic parameters E_M/E_O and G_M/G_O, k_M/k_O and the relative thermal conductivity σ_M/σ_O versus N are reported in Figs. 4-6, respectively.

From Figs. 4a and 4b, we can see that for all the t_0/l_0 ratios considered, the optimal E_M/E_O and G_M/G_O, which vary between 1 and 2, exist as N increases. Note that the optimal E_M/E_O and G_M/G_O may do not correspond to the same N. The reason is that E_O/E_s and E_M/E_h are independent of the Poisson's ratios ν_s and ν_h but G_O/G_s and G_M/G_h are dependent on them [51].

Figs. 5 and 6 show that the relative bulk modulus k_M/k_O and the relative thermal conductivity σ_M/σ_O increase with the increase of t_0/l_0, but they are generally less than 1 for all the t_0/l_0 ratios considered. This means that the effective bulk modulus and thermal conductivity of the MHH with regular hexagonal sub-structure are smaller than those of the ORHH structure. Of particular interest, there is an optimal value for the thermal conductivity, and this could be used to design low heat conductivity materials with an optimal topology.

3.3 The effects of t_0/l_0 – the cell-wall thickness-to-length ratio of the ORHH

To investigate the effects of the cell-wall thickness-to-length ratio t_0/l_0 of the ORHH on the relative elastic parameters and thermal conductivity of the MHH structure, again, we use the examples given in Section 3.2. We maintain $n=16$, $\lambda=0.02$ but change t_0/l_0 from 0.01 to 0.5 with the incremental step of 0.01. In fact, under the same N, the value of G_M/G_O is in general weakly larger than E_M/E_O (Fig. 4), so here we only consider the relative Young's modulus E_M/E_O against t_0/l_0. At the same time, σ_M/σ_O and k_M/k_O generally are smaller than 1 for all t_0/l_0 as those shown in Figs. 5 and 6, thus, the discussion will not be treated in this section.

Finally, the relationship between the maximum E_M/E_O and t_0/l_0 is reported in Fig. 7. We can see that the maximum E_M/E_O increases before t_0/l_0 reaches 0.07 but after that it decreases. That is to say, the optimal E_M/E_O of the MHH with hexagonal sub-structure exists at $t_0/l_0=0.07$, of which the value approximately equals to 2. This result is comparable to the finite element result given by Taylor et al. [49].

4. MHH with triangular sub-structure

4.1 Basic theory

In this section, we substitute the ORHH cell walls with the equal-mass isotropic triangular sub-structure, see Fig. 8. As defined in Section 3, the hierarchical length ratio is expressed as

$$\lambda=\frac{l_t}{l_0}=\frac{1}{n}\quad (n\geq 1) \tag{40}$$

where, n is the number of solid triangular lattice cell walls lying on the middle line of the MHH cell walls. From Fig. 8c, according to the equal-mass principle, we can find $t_0 l_0-\frac{1}{2\sqrt{3}}t_0^2=3\times\frac{1}{2}\left(t_t l_t-\frac{\sqrt{3}}{2}t_t^2\right)M$, which gives

$$\frac{t_t}{l_t}=\frac{1}{\sqrt{3}}\left[1-\sqrt{1-\frac{4\sqrt{3}}{3\lambda^2 M}\frac{t_0}{l_0}\left(1-\frac{1}{2\sqrt{3}}\frac{t_0}{l_0}\right)}\right] \tag{41}$$

where, M is the total number of half thickness triangular lattice cells in a MHH cell wall and it has the following relationship with n and N (see Appendix B):

$$M=2N\left(2n-N\right)+\frac{2}{3}\left(n-N\right)\quad(1\le N\le n) \tag{42}$$

in which N is the number of triangular lattice cells away from the middle line of the MHH cell walls. Similar to that in Section 3, a geometrical analysis on Fig. 8c provides $N_{\max}$, the upper bound of N, and t_1, the thickness of the MHH cell walls：

$$N_{\max}=n \tag{43}$$

$$t_1=\begin{cases}2N\left(\dfrac{\sqrt{3}}{2}l_t\right)+t_t & 1\le N\le N_{\max}-1\\ 2\times\dfrac{\sqrt{3}}{2}l_0 & N=N_{\max}\end{cases} \tag{44}$$

Then, rearranging Eq. (44) gives,

$$\frac{t_1}{l_0}=\begin{cases}\left(\sqrt{3}N+\dfrac{t_t}{l_t}\right)\lambda & 1\le N\le N_{\max}-1\\ \sqrt{3} & N=N_{\max}\end{cases} \tag{45}$$

On the other hand, with respect to Eq. (41), the relation $1-4\sqrt{3}\Big/\left(3\lambda^2 M\right)t_0/l_0\left[1-1\Big/\left(2\sqrt{3}\right)t_0/l_0\right]\ge 0$ should be satisfied. In conjunction with Eqs. (40) and (42), this relation gives $N_{\min}$, the lower bound of N：

$$N_{\min}=ce\left[\frac{6n-1-\sqrt{\left(6n-1\right)^2-12n\left[2\sqrt{3}n\dfrac{t_0}{l_0}\left(1-\dfrac{1}{2\sqrt{3}}\dfrac{t_0}{l_0}\right)-1\right]}}{6}\right] \tag{46}$$

Note that Eq. (46) may give $N_{\min}=0$, in this case $N_{\min}=1$.

Like the discussion in Section 3, we would like to analyze the effective elastic moduli and thermal conductivity of the triangular lattice sub-structure. As already mentioned in the introduction, Hyun and Torquato [11] showed that for triangular and Kagome honeycombs, both the in-plane effective moduli and conductivity (or dielectric constant) are approaching the H-S upper bounds [12-13]. So, we approximately use the H-S upper bounds to calculate the effective elastic moduli and thermal conductivity of the triangular lattice sub-structure. Defining the in-plane Young's, shear and bulk moduli and thermal conductivity of the triangular sub-structure as E_t, G_t, k_t and σ_t, we obtain:

$$\frac{E_t}{E_s} = A_t = \frac{\phi_t}{3-2\phi_t} \tag{47}$$

$$\frac{k_t}{k_s} = B_t = \frac{\phi_t G_s/k_s}{1-\phi_t+G_s/k_s} \tag{48}$$

$$\frac{G_t}{E_s} = C_t = \frac{1}{2(1+\nu_s)}\frac{\phi_t}{(1-\phi_t)(1+2G_s/k_s)+1} \tag{49}$$

$$\frac{\sigma_t}{\sigma_s} = \frac{\phi_t}{2-\phi_t} \tag{50}$$

where,

$$\phi_t = 2\sqrt{3}\frac{t_t}{l_t} - 3\left(\frac{t_t}{l_t}\right)^2 \left(\frac{t_t}{l_t} \le \frac{1}{\sqrt{3}}\right) \tag{51}$$

is the relative density of the triangular sub-structure. Denoting the effective Poisson's ratio of the triangular sub-structure by ν_t, the relation $G_t = E_t/[2(1+\nu_t)]$ holds. Then, combining Eqs. (47) and (49) gives,

$$\nu_t = \frac{1}{2}\frac{A_t}{C_t} - 1 \tag{52}$$

Thus,

$$\frac{G_t}{k_t} = \frac{E_t/[2(1+\nu_t)]}{E_t/[2(1-\nu_t)]} = \frac{1-\nu_t}{1+\nu_t} = 4\frac{C_t}{A_t} - 1 \tag{53}$$

At the same time, by treating the triangular sub-structure as a continuum and defining the in-plane Young's, shear and bulk moduli and thermal conductivity of the MHH with triangular sub-structure as E_M, G_M, k_M and σ_M, we have:

$$\frac{E_M}{E_t} = A_M = \begin{cases} \dfrac{3}{2}\phi_M^3 & \phi_M \le 0.5 \\ \dfrac{\phi_M(2\zeta_M - 1)(\zeta_M + \eta_M - 1)}{\left\{3 - 2\phi_M - 2(2-\phi_M)(1-\zeta_M) + (2-\zeta_M-\eta_M)\left[2\phi_M(1-\zeta_M)-1\right]\right\}} & \phi_M > 0.5 \end{cases} \tag{54}$$

$$\frac{k_M}{k_t} = B_M = \frac{G_t/k_t\,\phi_M(2\zeta_M - 1)}{(1-\phi_M) + G_t/k_t\left[1 + 2\phi_M(\zeta_M - 1)\right]} \tag{55}$$

$$\frac{G_M}{E_t} = \frac{A_M B_M}{4B_M - 2A_M(1-\nu_t)} \tag{56}$$

$$\frac{\sigma_M}{\sigma_t} = \frac{\phi_M}{2-\phi_M} \tag{57}$$

where,

$$\phi_M = \frac{2}{\sqrt{3}}\frac{t_1}{l_0} - \frac{1}{3}\left(\frac{t_1}{l_0}\right)^2 \quad \left(\frac{t_1}{l_0} \le \sqrt{3}\right) \tag{58}$$

and ζ_M and η_M, interpolated from Fig. 1a, are the three-point parameters corresponding to ϕ_M.

Combining Eqs. (19), (47) and (54) gives the relative Young's modulus E_M/E_O:

$$\frac{E_M}{E_O} = \frac{A_M A_t}{A_O} \tag{59}$$

Similarly, from Eqs. (20), (48) and (55), we can find the relative bulk modulus k_M/k_O:

$$\frac{k_M}{k_O} = \frac{B_M B_t}{B_O} \tag{60}$$

And from Eqs. (21), (47) and (56), we obtain the relative shear modulus G_M/G_O:

$$\frac{G_M}{G_O} = \frac{A_M B_M A_t}{2B_M - A_M(1-\nu_t)} \frac{2B_O - A_O(1-\nu_s)}{A_O B_O} \tag{61}$$

Finally, from Eqs. (23), (50) and (57), the relative thermal conductivity σ_M/σ_O is derived:

$$\frac{\sigma_M}{\sigma_O}=\frac{\phi_M\phi_t(2-\phi_O)}{\phi_O(2-\phi_M)(2-\phi_t)} \tag{62}$$

4.2 Effects of N on the relative elastic moduli and thermal conductivity of the MHH with triangular sub-structure

As discussed in Section 3, the influence of N on the effective elastic moduli and thermal conductivity of the MHH with triangular sub-structure are studied, here we consider other examples with parameters $n=20$, $\lambda=1/n=0.05$, $t_0/l_0=0.01$, 0.05, 0.1, 0.2 and 0.3. Then, we immediately obtain $N_{\max}=20$ by Eq. (23) and the lower bound $N_{\min}$ for each t_0/l_0 by Eq. (46). The results of the relative elastic moduli E_M/E_O, G_M/G_O, k_M/k_O and the relative thermal conductivity σ_M/σ_O versus N are reported in Figs. 9-12, respectively.

From Figs. 9 and 10, we can also see that the relative Young's modulus E_M/E_O and the effective shear modulus G_M/G_O increase with the increase of N, and the thickness-to-length ratio t_0/l_0 has a strong influence on them. With respect to its equal-mass ORHH, the enhancements of the relative Young's and shear moduli of the MHH with triangular sub-structure can be 1 order (Figs. 9c and 10c) or even 3 orders of magnitude (Figs. 9a and 10a). Although the enhancement on Young's modulus of the MHH with triangular sub-structure decreases with the increase of t_0/l_0, for a relatively small t_0/l_0 (less than 0.3), its stiffening effect (Figs. 9 and 10) by the triangular sub-structure is much larger than that of the hexagonal sub-structure (Figs. 4a, b).

The relative bulk modulus k_M/k_O and the relative thermal conductivity σ_M/σ_O shown in Figs. 11 and 12 have the same varying trends with those of the MHH with hexagonal sub-structure reported in Section 3.2. The discussion is the same as before.

5. MHH with isotropic Kagome sub-structure

5.1 Basic theory

Kagome honeycomb has been revealed to have pronounced higher fracture toughness [30] and

better thermal-mechanical performance than the triangular honeycombs [54]. Therefore, in this section, we will consider the third topology of the MHH, namely, substituting the ORHH cell walls with their equal-mass Kagome sub-structure (Fig. 13), and study its effective elastic moduli and thermal conductivity. In this case, the hierarchical length ratio is expressed as:

$$\lambda = \frac{l_k}{l_0} = \frac{1}{n} \quad n = 4,\ 6,\ 8,\ 10\ \cdots \tag{63}$$

where, l_k is the side length of triangles in Kagome cells and n is the number of sides of the effective triangles on the middle line of the MHH cell walls. As discussed before, here, the equal-mass principle provides $t_0 l_0 - \frac{1}{2\sqrt{3}} t_0^2 = 3\times\left(t_k l_k - \frac{\sqrt{3}}{2} t_k^2 \right) M$, and t_k / l_k is derived as:

$$\frac{t_k}{l_k} = \frac{1}{\sqrt{3}}\left[1 - \sqrt{1 - \frac{2\sqrt{3}}{3\lambda^2 M}\frac{t_0}{l_0}\left(1 - \frac{1}{2\sqrt{3}}\frac{t_0}{l_0} \right)} \right] \tag{64}$$

where, M is the total number of triangles in a MHH cell wall, and it is expressed with n and N as (see Appendix C):

$$M = 2N\left(n - N \right) \quad \left(1 \le N \le \frac{n}{2} \right) \tag{65}$$

in which N is the number of the Kagome representative cells (e.g., in Fig. 13c, $N = 1$) away from the middle line of the MHH cell walls. Similar to that in Sections 3 and 4, a geometrical analysis on Fig. 13c provides $N_{\max}$, the upper bound of N, and t_1, the thickness of the MHH cell walls：

$$N_{\max} = \frac{n}{2} \tag{66}$$

$$t_1 = \begin{cases} 2N\left(\sqrt{3} l_k \right) + 2t_k & 1 \le N \le N_{\max} - 1 \\ 2\times\frac{\sqrt{3}}{2} l_0 & N = N_{\max} \end{cases} \tag{67}$$

Then, rearranging Eq. (67) gives

$$\frac{t_1}{l_0}=\begin{cases}2\left(\sqrt{3}N+\dfrac{t_k}{l_k}\right)\lambda & 1\le N\le N_{\max}-1\\ \sqrt{3} & N=N_{\max}\end{cases} \tag{68}$$

On the other hand, with respect to Eq. (64), the relation $1-2\sqrt{3}/\left(3\lambda^2 M\right)t_0/l_0\left[1-1/\left(2\sqrt{3}\right)t_0/l_0\right]\ge 0$ holds. In conjunction with Eqs. (63) and (65), this relation gives $N_{\min}$, the lower bound of N:

$$N_{\min}=ce\left[\frac{n-n\sqrt{1-\dfrac{4\sqrt{3}}{3}\dfrac{t_0}{l_0}\left(1-\dfrac{1}{2\sqrt{3}}\dfrac{t_0}{l_0}\right)}}{2}\right] \tag{69}$$

Also, it should be note that Eq. (69) may give $N_{\min}=0$, for this case $N_{\min}=1$.

Here, we again approximately use the H-S upper bounds to analyze the effective elastic moduli and thermal conductivity of the Kagome lattice sub-structure. Defining the in-plane Young's, shear and bulk moduli and thermal conductivity of the Kagome sub-structure as E_k, G_k, k_k and σ_k, we obtain:

$$\frac{E_k}{E_s}=A_k=\frac{\phi_k}{3-2\phi_k} \tag{70}$$

$$\frac{k_k}{k_s}=B_k=\frac{\phi_k G_s/k_s}{1-\phi_k+G_s/k_s} \tag{71}$$

$$\frac{G_k}{E_s}=C_k=\frac{1}{2\left(1+\nu_s\right)}\frac{\phi_k}{\left(1-\phi_k\right)\left(1+2G_s/k_s\right)+1} \tag{72}$$

$$\frac{\sigma_k}{\sigma_s}=\frac{\phi_k}{2-\phi_k} \tag{73}$$

where,

$$\phi_k=\sqrt{3}\frac{t_k}{l_k}-\left(\frac{t_k}{l_k}\right)^2\quad\left(\frac{t_k}{l_k}\le\frac{1}{\sqrt{3}}\right) \tag{74}$$

is the relative density of the Kagome sub-structure. Denoting the effective Poisson's ratio of the

Kagome sub-structure by ν_k, employing $G_k = E_k/\left[2(1+\nu_k)\right]$ and combining Eqs. (70) and (72) give

$$\nu_k = \frac{1}{2}\frac{A_k}{C_k} - 1 \tag{75}$$

Thus,

$$\frac{G_k}{k_k} = \frac{E_k/\left[2(1+\nu_k)\right]}{E_k/\left[2(1-\nu_k)\right]} = \frac{1-\nu_k}{1+\nu_k} = 4\frac{C_k}{A_k} - 1 \tag{76}$$

Again, by treating the Kagome sub-structure as a continuum and defining the in-plane Young's, shear and bulk moduli and thermal conductivity of the MHH with Kagome sub-structure as E_M, G_M, k_M and σ_M, we have:

$$\frac{E_M}{E_k} = A_M = \begin{cases} \dfrac{3}{2}\phi_M^3 & \phi_M \le 0.5 \\ \dfrac{\phi_M(2\zeta_M - 1)(\zeta_M + \eta_M - 1)}{\left\{3 - 2\phi_M - 2(2-\phi_M)(1-\zeta_M) + (2-\zeta_M-\eta_M)\left[2\phi_M(1-\zeta_M) - 1\right]\right\}} & \phi_M > 0.5 \end{cases} \tag{77}$$

$$\frac{k_M}{k_k} = B_M = \frac{G_k/k_k\,\phi_M(2\zeta_M - 1)}{(1-\phi_M) + G_k/k_k\left[1 + 2\phi_M(\zeta_M - 1)\right]} \tag{78}$$

$$\frac{G_M}{E_k} = \frac{A_M B_M}{4B_M - 2A_M(1-\nu_k)} \tag{79}$$

$$\frac{\sigma_M}{\sigma_k} = \frac{\phi_M}{2-\phi_M} \tag{80}$$

where,

$$\phi_M = \frac{2}{\sqrt{3}}\frac{t_1}{l_0} - \frac{1}{3}\left(\frac{t_1}{l_0}\right)^2 \quad \left(\frac{t_1}{l_0} \le \sqrt{3}\right) \tag{81}$$

and ζ_M and η_M interpolated from Fig. 1a are the three-point parameters corresponding to ϕ_M.

Combining Eqs. (19), (70) and (77) gives the relative Young's modulus E_M/E_O:

$$\frac{E_M}{E_O} = \frac{A_M A_k}{A_O} \tag{82}$$

Similarly, from Eqs. (20), (71) and (78) we can get the relative bulk modulus k_M/k_O:

$$\frac{k_M}{k_O}=\frac{B_M B_k}{B_O} \tag{83}$$

And from Eqs. (21), (70) and (79) we obtain the relative shear modulus G_M/G_O:

$$\frac{G_M}{G_O}=\frac{A_M B_M A_k}{2B_M-A_M(1-\nu_k)}\frac{2B_O-A_O(1-\nu_s)}{A_O B_O} \tag{84}$$

Finally, from Eqs. (23), (50) and (57), we find the relative thermal conductivity σ_M/σ_O:

$$\frac{\sigma_M}{\sigma_O}=\frac{\phi_M\phi_k(2-\phi_O)}{\phi_O(2-\phi_M)(2-\phi_k)} \tag{85}$$

5.2 Effects of N on the relative elastic moduli and thermal conductivity of the MHH with Kagome sub-structure

In this section, we consider the examples with parameters $n=20$, $\lambda=1/n=0.05$, $t_0/l_0=0.01$, 0.05, 0.1, 0.2 and 0.3. Then, Eq. (66) provides $N_{\max}=10$ and Eq. (69) the lower bound $N_{\min}$ for each t_0/l_0. The results of the relative elastic moduli E_M/E_O, G_M/G_O, k_M/k_O and the relative thermal conductivity σ_M/σ_O versus N are shown in Figs. 14-17, respectively.

Comparing Figs. 14 and 15 with Figs. 9 and 10, we can see that the Young's and shear moduli of the MHH with Kagome sub-structure are similar to those of the MHH with triangular sub-structure, so the discussion is the same as before.

However, it is worth to say that, different from the MHH with hexagonal and triangular sub-structures, the relative bulk modulus k_M/k_O and the relative thermal conductivity σ_M/σ_O of the MHH with Kagome sub-structure become larger than 1 with the increase of t_0/l_0 (Figs. 16 and 17). This is to say, when t_0/l_0 is large enough, the effective bulk modulus and thermal conductivity of the MHH with Kagome sub-structure could be greater than those of the ORHH structures.

6. Comparisons of hexagonal, triangular and Kagome sub-structures

Comparing the examples discussed in Sections 3 to 5, it is apparent that for the same ORHH,

the in-plane stiffness enhancements of the MHH with triangular and Kagome sub-structures could be much greater than that with the hexagonal sub-structure. To illustrate this point clearly, one more example with the parameters $t_0/l_0 = 0.1$ and $\lambda = 1/20$ is analyzed, and the result is plotted in Fig. 18, in which the relative Young's modulus E_M/E_O against N for the MHH with the above three sub-structures are depicted. Interestingly, we find that the relative Young's moduli of the MHH with triangular and Kagome sub-structures increase as *N* increases, but it is inverse for the MHH with hexagonal sub-structure. And more, the Young's modulus of the MHH with Kagome sub-structure is improved most with respect to the ORHH.

For the comparisons on bulk modulus and thermal conductivity of the three MHHs, the parameters $t_0/l_0 = 0.3$ and $\lambda = 1/20$ are employed, and the results are depicted in Figs. 19 and 20. From the two figures, we can say that the MHH with Kagome sub-structure is the optimal structure to design the elastic moduli and transport properties of the multifunctional regular hexagonal honeycomb.

7. Conclusions

In this paper, we have studied the in-plane elastic and transport properties of the MHH, which is formed by replacing the ORHH solid cell walls with three types of equal-mass isotropic honeycomb sub-structures. The analytical results show that with the hexagonal sub-structure it is difficult to greatly increase the Young's and shear moduli of the MHH. Different from the hexagonal sub-structure, triangular and Kagome sub-structures share a similar improvement on the MHH's Young's and shear moduli, and the improvement is substantial, from 1 order to 3 orders of magnitude depending on the cell-wall thickness-to-length ratio t_0/l_0 of the ORHH. At the same time, if t_0/l_0 is large enough, the effective bulk modulus and transport ability of the MHH with Kagome sub-structure can be larger than those of the ORHH structure. These interesting results show a possibility to design hierarchical honeycombs for multifunctional applications, e.g., the metal MHH can be used as the core of light weight sandwich panels in electronic packages and

airborne devices, where both the structural and thermal characteristics are desirable.

Acknowledgements

The research related to these results has received funding from the European Research Council under the European Union's Seventh Framework Programme (FP7/2007-2013)/ERC Grant agreement nu [279985] (ERC Starting Grant, PI NMP on "Bio-inspired hierarchical super nanomaterials"). Y. Sun and Q. Chen appreciate the China Scholarship Council (CSC) for the financial supports.

Appendix A: MHH cell wall with hexagonal sub-structures

Fig. A.1 shows the representative cell walls of the MHH with regular hexagonal sub-structures shown in Fig. 3b. The mass of the sub-structure is distributed uniformly among the half-thickness hexagonal sub-structure cells within the blue hexagon.

From Fig. A.1 we can see that the number of the half-thickness hexagonal sub-structure cells M can be determined by n and N as the following form:

$$M = 2N\left[n+(n+1)\right]+\frac{1}{6}(2n)-4A_N = 2N(2n+1)+\frac{n}{3}-4A_N \tag{A.1}$$

in which $A_1 = 1/6$ and $A_2 = 1$.

Here, A_N depends on N, we find it generally expressed as:

$$A_N = \frac{(2N+1)(N-1)+1}{6} \quad (N \geq 1) \tag{A.2}$$

Appendix B: MHH cell wall with triangular sub-structures

Fig. B.1 schematically shows the cell walls of the MHH with triangular sub-structures (Fig. 8b).The hierarchical length ratio is $\lambda = 1/n$. M is the total number of the half-thickness triangular cells in one sub-structure cell wall. It is easy to get the following relation between M, N and n:

$$\begin{aligned} &N=1:\ M = 2(2n\times 1-1)+\frac{2}{3}(n-1)\\ &N=2:\ M = 2(2n\times 2-1-1-2)+\frac{2}{3}(n-2)\\ &N=3:\ M = 2(2n\times 3-1-1-2-2-3)+\frac{2}{3}(n-3) \end{aligned} \tag{B.1}$$

Then, by inductive method, we find:

$$M = 2(2n\times N - B_N)+\frac{2}{3}(n-N) \quad 1 \leq N \leq n \tag{B.2}$$

with

$$B_N = N^2 \tag{B.3}$$

Substituting Eq. (B.3) into Eq. (B.2) gives:

$$M = 2N\left(2n-N\right)+\frac{2}{3}\left(n-N\right) \quad (1\le N\le n) \tag{B.4}$$

Appendix C: MHH cell wall with Kagome sub-structures

Fig. C.1 schematically shows the cell walls of the MHH with Kagome sub-structures. The hierarchical length ratio is $\lambda = 1/n$. M is the total number of the triangular cells contained in one Kagome sub-structure cell wall. Then, the relationship between M, N and n are expressed as:

$$\begin{aligned} &N=1:\ M=2\left[\left(n-1\right)-0\right] \\ &N=2:\ M=2\left[2\left(n-1\right)-2\right] \\ &N=3:\ M=2\left[3\left(n-1\right)-2-4\right] \end{aligned} \tag{C.1}$$

Then, by inductive method, we find:

$$M = 2\left[N\left(n-1\right)-C_N\right] \ \ 1\le N\le \frac{n}{2} \tag{C.2}$$

with

$$C_N = N\left(N-1\right) \tag{C.3}$$

Substituting Eq. (C.3) into Eq. (C.2) gives:

$$M = 2N\left(n-N\right) \quad (1\le N\le \frac{n}{2}) \tag{C.4}$$

References

1. Huang JS, Gibson LJ. Microstructural design of cellular materials—I: honeycomb beams and plates. Acta Metallurgica et Materialia 1994;43(4):1643-1650.

2. Masters IG, Evans KE. Models for the elastic deformation of honeycombs. Composite Structures 1996;35(4):403-422.

3. Gibson LJ, Ashby MF. Cellular Solids, Structures and Properties-2nd ed. Cambridge: Cambridge University Press, 1997.

4. Wilson S. A new face of aerospace honeycomb. Materials and Design 1990;11(6):323-326.

5. Bitzer T. Honeycomb marine applications. Journal of Reinforced Plastics and Composites 1994;13(4):355-360.

6. Thompson RW, Matthews FL. Load attachments for honeycomb panels in racing cars. Materials and Design 1995;16(3):131-150.

7. Price T, Timbrook RL. Structural honeycomb panel building system, Patent number US6, 253, 530 B1. Jul. 3,2001.

8. Lu TJ. Heat transfer efficiency of metal honeycombs. International Journal of Heat and Mass Transfer 1999;42(11):2031-2040.

9. Gu S, Lu TJ, Evans AG. On the design of two-dimensional cellular metals for combined heat dissipation and structural load capacity. International Journal of Heat and Mass Transfer 2001;44(11):2163-2175.

10. Wen T, Tian J, Lu TJ, Queheillalt DT, Wadley HNG. Forced convection in metallic honeycomb structures. International Journal of Heat and Mass Transfer 2006;49:3313-3324.

11. Hyun S, Torquato S, Optimal and manufacturable two-dimensional, Kagome-like cellular solids. Journal of Materials Research 2002;17(1):137-144.

12. Hashin Z, Shtrikman S. A variational approach to the theory of the effective magnetic permeability of multiphase materials. Journal of Applied Physics 1962;33(10) :3125- 3131.

13. Hashin Z, Shtrikman S. A variational approach to the theory of the elastic behaviour of multiphase materials. Journal of the Mechanics and Physics of Solids 1963;11(2):127-140.

14. Evans AG, Hutchinson JW, Fleck NA, Ashby MF, Wadley HNG. The topology design of multifunctional cellular metals. Progress in Materials Science 2001;46:309-327.

15. Wadley HNG, Fleck NA, Evans AG. Fabrication and structural performance of periodic cellular metal sandwich structures. Composites Science and Technology 2003;63(16):2331-2343.

16. Wadley HNG. Multifunctional periodic cellular metals. Philosophical Transactions of the Royal Society A 2006;364(1838):31-68.

17. Hayes AM, Wang A, Dempsey BM, McDowell DL. Mechanics of linear cellular alloys. Mechanics of Materials 2004;36(8):691-713.

18. Mohr D, Xue Z, Vaziri A. Quasi-static punch indentation of a honeycomb sandwich plate: experiments and modeling. Journal of Mechanics of Materials and Structures 2006;1(3):581-604.

19. Vaziri A, Hutchinson JW. Metal sandwich plates subject to intense air shocks. International Journal of Solids and Structures 2007;44:2021-2035.

20. Vaziri A, Xue Z, Hutchinson JW. Performance and failure of metal sandwich plates subject to shock loading. Journal of Mechanics of Materials and Structures 2007; 2(10):1947-1963.

21. Ebrahimi H, Vaziri A. Metallic sandwich panels subjected to multiple intense shocks. International Journal of Solids and Structures 2013;50:1164-1176.

22. Mori LF, Lee S, Xue ZY, Vaziri A, Queheillalt DT, Dharmasena KP, Wadley HNG, Hutchinson JW, Espinosa HD. Deformation and fracture modes of sandwich structures subjected to underwater impulsive loads. Journal of Mechanics of Materials and Structures 2007; 2(10):1981-2006.

23. Wadley HNG, Dharmasena KP, Queheillalt DT, Chen Y, Dudt P, Knight D, Kiddy K, Xue Z, Vaziri A. Dynamic compression of square honeycomb structures during underwater impulsive loading. Journal of Mechanics of Materials and Structures 2007; 2(10): 2025-2048.

24. Babaee S, Jahromi BH, Ajdari A, Nayeb-Hashemi H, Vaziri A. Mechanical properties of open-cell rhombic dodecahedron cellular structures. Acta Materialia 2012; 60: 2873-2885.

25. Xiong J, Ma L, Wu L, Wang B, Vaziri A. Fabrication and crushing behavior of low density carbon fiber composite pyramidal truss structures. Composite Structures 2010; 92(11): 2695-2702.

26. Xiong J, Ma L, Wu L, Liu J, Vaziri A. Mechanical behavior and failure of composite pyramidal truss core sandwich columns. Composites: Part B 2011; 42: 938-945.

27. Xiong J, Vaziri A, Ma L, Papadopoulos J, Wu L. Compression and impact testing of two-layer composite pyramidal-core sandwich panels. Composite Structures 2012; 94(2): 793-801.

28. Xiong J, Ma L, Pan S, Wu L, Papadopoulos J, Vaziri A. Shear and bending performance of carbon fiber composite sandwich panels with pyramidal truss cores. Acta Materialia 2012, 60:1455-1466.

29. Wang AJ, McDowell DL. In-plane stiffness and yield strength of the periodic metal honeycombs. Journal of Engineering Materials and Technology 2004;126(2):137-156.

30. Fleck NA, Qiu X. The damage tolerance of elastic-brittle, two-dimensional isotropic lattices. Journal of the Mechanics and Physics of Solids 2007;55(3):562-588.

31. Lakes R. Materials with structural hierarchy. Nature 1993;361:511-515.

32. Pugno N. Mimicking nacre with super-nanotubes for producing optimized super-composites. Nanotechnology 2006;17(21):5480-5484.

33. Gao H. Application of fracture mechanics concepts to hierarchical biomechanics of bone and bone-like materials. International Journal of Fracture 2006;138:101-137.

34. Pugno N, Carpinteri A. Design of micro-nanoscale bio-inspired hierarchical materials. Philosophical Magazine Letters 2008;88(6): 397-405.

35. Carpinteri A, Pugno N. Mechanics of hierarchical materials. International Journal of Fracture 2008;150:221-226.

36. Zhao Q, Kreplak L, Buehler MJ. Hierarchical Structure Controls Nanomechanical Properties of Vimentin Intermediate Filaments. PLoS ONE 2009;4(10):e7294.

37. Fratzl P, Weinkamer R. Nature's hierarchical materials. Progress in Materials Science 2007;52: 1263-1334.

38. Pugno N, Chen Q. In plane elastic properties of hierarchical cellular solids. Engineering Procedia, Physics Engineering 2011;10,3026-3031.

39. Chen Q, Pugno N. Modeling the elastic anisotropy of woven hierarchical tissues. Composites Part B: Engineering 2011;42(7):2030-2037.

40. Chen Q, Huang S. Mechanical properties of a porous bioscaffold with hierarchy. Materials Letters 2013;95:89-92.

41. Chen Q, Pugno NM. Bio-mimetic mechanisms of natural hierarchical materials: A review. Journal of the Mechanical Behavior of Biomedical Materials 2013; 19: 3-33.

42. Chen Q, Pugno N. Mechanics of hierarchical 3-D nanofoams. Europhysics Letters 2012; 97:26002.

43. Chen Q, Pugno N. In-plane elastic buckling of hierarchical honeycomb materials, European Journal of Mechanics A/Solids 2012;34:120-129.

44. Chen Q, Pugno N. Competition between in-plane buckling and bending collapses in nano-honeycombs. Europhysics Letters 2012;98:16005.

45. Burgueno R, Quagliata MJ, Mohanty AK, Mehtad G, Drzale LT, Misraf M. Hierarchical cellular designs for load-bearing biocomposite beams and plates. Materials Science and Engineering: A 2005;390:178-187.

46. Kooistra GW, Deshpande V, Wadley HNG. Hierarchical corrugated core sandwich panel concepts. Journal of Applied Mechanics 2007;74(2): 259-268.

47. Fan HL, Jin FN, Fang DN. Mechanical properties of hierarchical cellular materials. Part I: Analysis. Composite Science and Technology 2008;68:3380-3387.

48. Garcia AP, Pugno N, Buehler MJ. Superductile, wavy silica nanostructures inspired by diatom algae. Advanced Engineering Materials 2011;13(10):B405-B414.

49. Taylor CM, Smith CW, Miller W, Evans KE. The Effects of hierarchy on the in-plane elastic properties of honeycombs. International Journal of Solids and Structures 2011;48(9):1330-1339.

50. Ajdari A, Jahromi BH, Papadopoulos J, Nayeb-Hashemi H, Vaziri A. Hierarchical honeycombs with tailorable properties. International Journal of Solids and Structures 2012;49:1413-1419.

51. Hyun S, Torquato S. Effective and transport properties of regular honeycombs for all densities. Journal of Materials Research 2000;15(9): 1985-1993.

52. Torquato S, Gibiansky LV, Silva MJ, Gibson LJ. Effective mechanical and transport properties of cellular solids. International Journal of Mechanical Sciences 1998;40(1):71-82.

53. Jasiuk I, Chen J, Thorpe MF. Elastic moduli of two dimensional materials with polygonal and elliptical holes. Applied Mechanics Reviews 1994;47 (1):S18-S28.

54. Wang Bo, Wang Bin, Cheng G. Multifunctional design of sandwich panels with Kagome-like cores. Acta Materiae Compositae Sinica 2007; 24(3):109-115.

Figure Captions:

Fig. 1 (a) Three-point parameters ζ and η for the regular hexagonal honeycomb [51] (Hyun and Torquato, 2000) *vs* the relative density ϕ; (b) Effective Young's modulus E_e/E_s of the regular hexagonal honeycomb *vs* the relative density ϕ predicted by different methods.

Fig. 2 The effective Poisson's ratio ν_e of the regular hexagonal honeycomb with $\nu_s = 1/3$ *vs* the relative density ϕ.

Fig. 3 (a) The original regular hexagonal honeycomb (ORHH); (b) the tailorable multifunctional hierarchical honeycomb (MHH) with hexagonal sub-structure; (c) amplification of a hexagonal lattice cell wall in (b) (the cell walls marked by blue circle suggest *n*=8 and the dash line denotes the middle line of the MHH cell wall).

Fig. 4 (a) The relative Young's modulus E_M/E_O *vs* N for different t_0/l_0; (b) The relative shear modulus G_M/G_O *vs* N for different t_0/l_0.

Fig. 5 The relative bulk modulus G_M/G_O *vs* N for different t_0/l_0

Fig. 6 The relative thermal conductivity G_M/G_O *vs* N for different t_0/l_0

Fig. 7 The maximum E_M/E_O vs t_0/l_0

Fig. 8 Schematics of (a) the ORHH; (b) the tailorable MHH with triangular sub-structure; (c) amplification of a trianglar lattice cell wall in (b).

Fig. 9 The relative Young's modulus E_M/E_O *vs* N for different t_0/l_0 : (a) $t_0/l_0 = 0.01$; (b) $t_0/l_0 = 0.05$; (c) $t_0/l_0 = 0.1, 0.2, 0.3$.

Fig. 10 The relative Young's modulus G_M/G_O *vs* N for different t_0/l_0 : (a) $t_0/l_0 = 0.01$; (b) $t_0/l_0 = 0.05$; (c) $t_0/l_0 = 0.1, 0.2, 0.3$.

Fig. 11 The relative bulk modulus k_M/k_O vs N for different t_0/l_0

Fig. 12 The relative thermal conductivity σ_M/σ_O *vs* N for different t_0/l_0

Fig. 13 Schematics of (a) the ORHH; (b) the tailorable MHH with Kagome sub-structure (in this paper the red dashline is for the convenience of linear dimension); (c) amplication of a Kagome sub-structure cell wall in (b); (d) the representative cells for the Kagome honeycomb.

Fig. 14 The relative Young's modulus E_M/E_O *vs* N for different t_0/l_0 : (a) $t_0/l_0=0.01$; (b) $t_0/l_0=0.05$; (c) $t_0/l_0=0.1, 0.2, 0.3$.

Fig. 15 The relative Young's modulus G_M/G_O *vs* N for different t_0/l_0 : (a) $t_0/l_0=0.01$; (b) $t_0/l_0=0.05$; (c) $t_0/l_0=0.1, 0.2, 0.3$.

Fig. 16 The relative bulk modulus k_M/k_O *vs* N for different t_0/l_0

Fig. 17 The relative thermal conductivity σ_M/σ_O *vs* N for different t_0/l_0

Fig. 18 The relative Young's modulus E_M/E_O *vs* N for different sub-structures with the same parameters $t_0/l_0=0.1$ and $\lambda=1/20$.

Fig. 19 The relative bulk modulus k_M/k_O *vs* N for different sub-structures with the same parameters $t_0/l_0=0.3$ and $\lambda=1/20$.

Fig. 20 The relative thermal conductivity σ_M/σ_O *vs* N for different sub-structures with the same parameters $t_0/l_0=0.3$ and $\lambda=1/20$.

Fig. A.1 Schematics of MHH cell walls in Fig. 1b: (a) $N=1$; (b) $N=2$.

Fig. B.1 Schematics for the representative cell walls of the MHH with triangular sub-structures: (a) $N=1$; (b) $N=2$.

Fig. C.1 Schematics for the representative cell walls of the MHH with Kagome sub-structures: (a) $N=1$; (b) $N=2$.

Figure 1

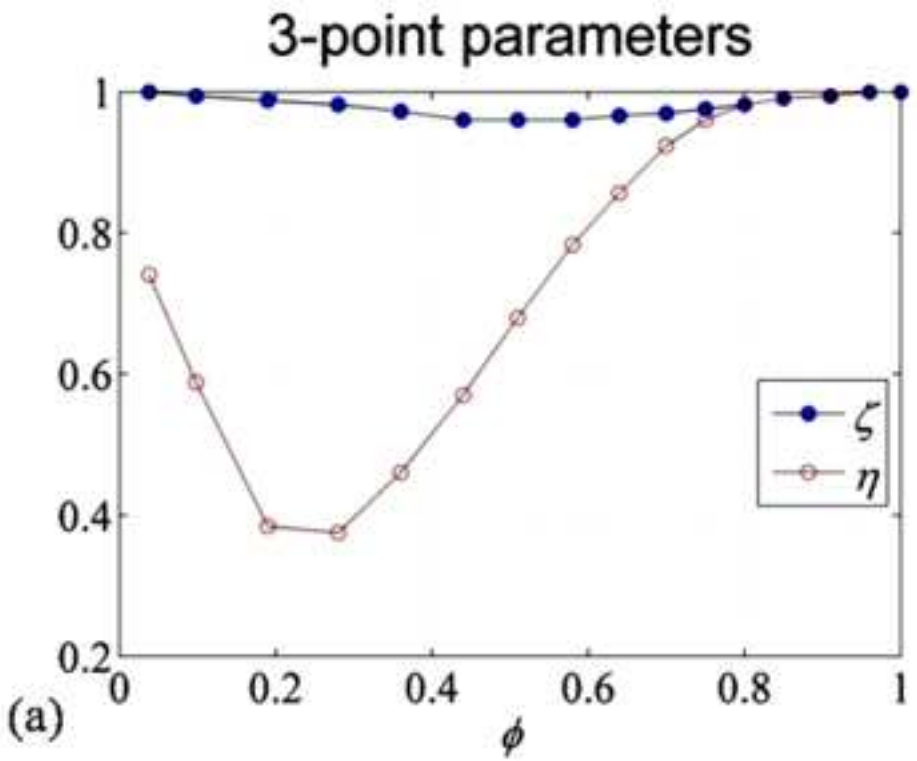

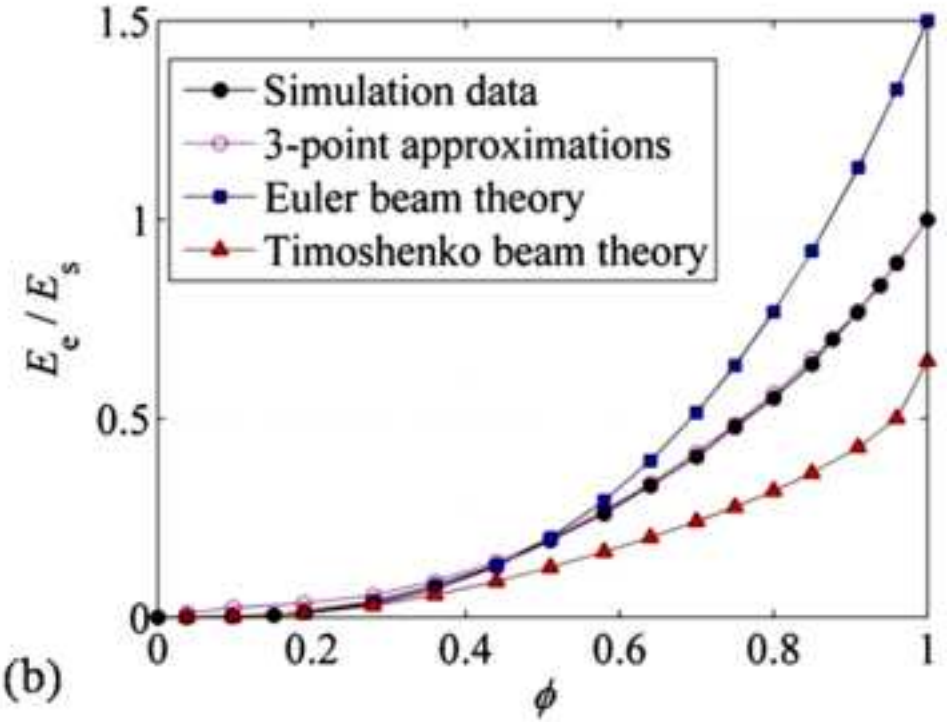

Figure 2

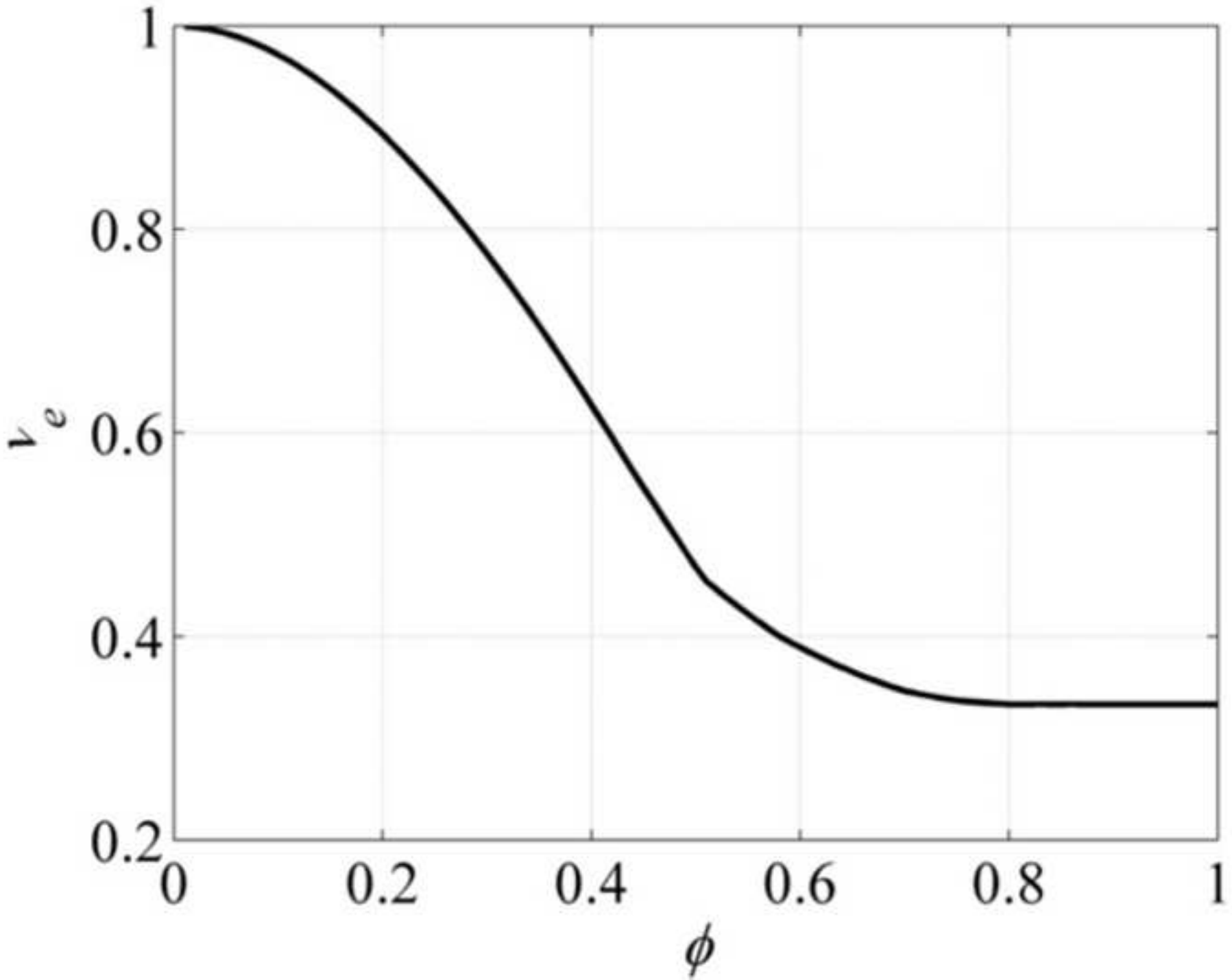

Figure 3

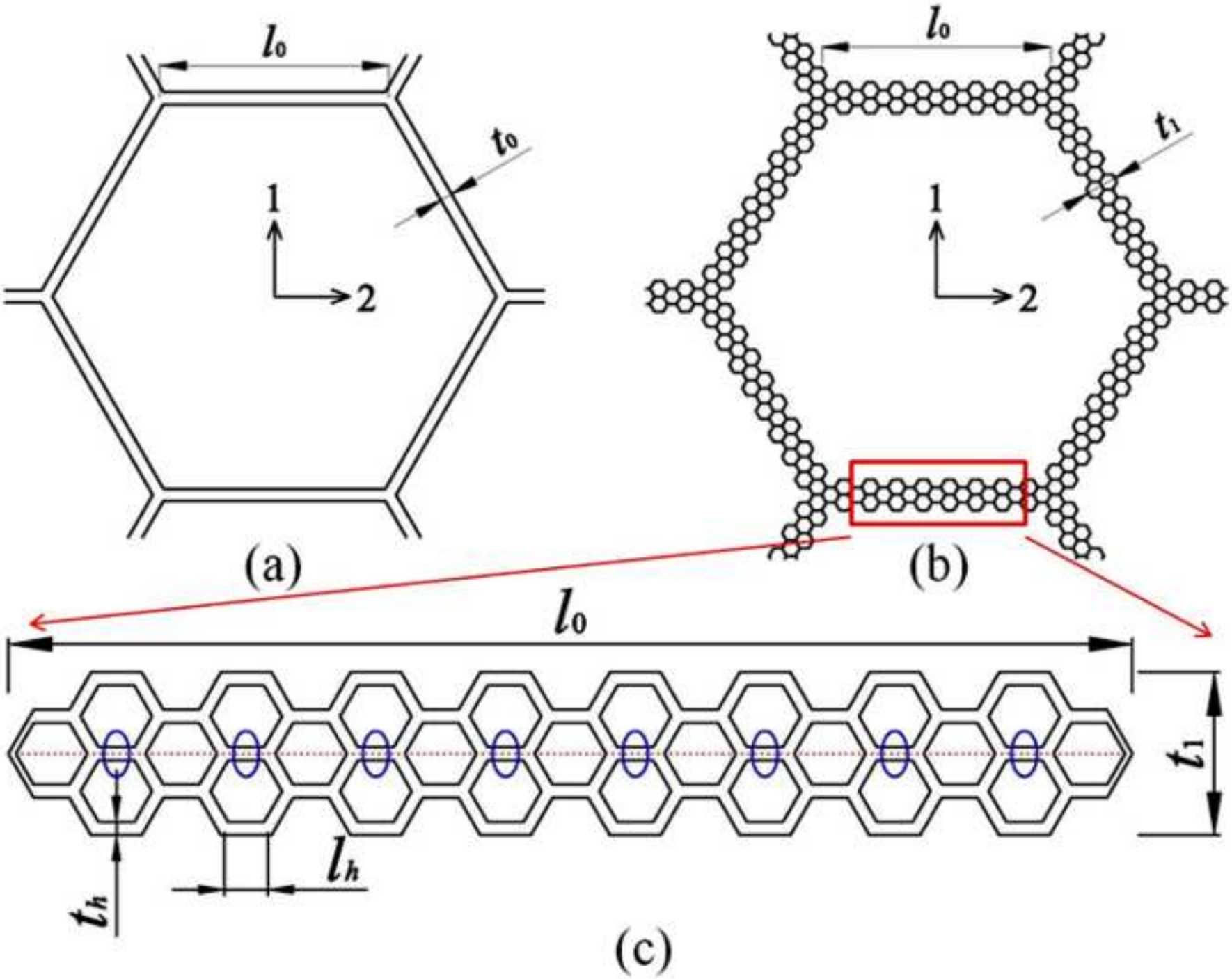

Figure 4

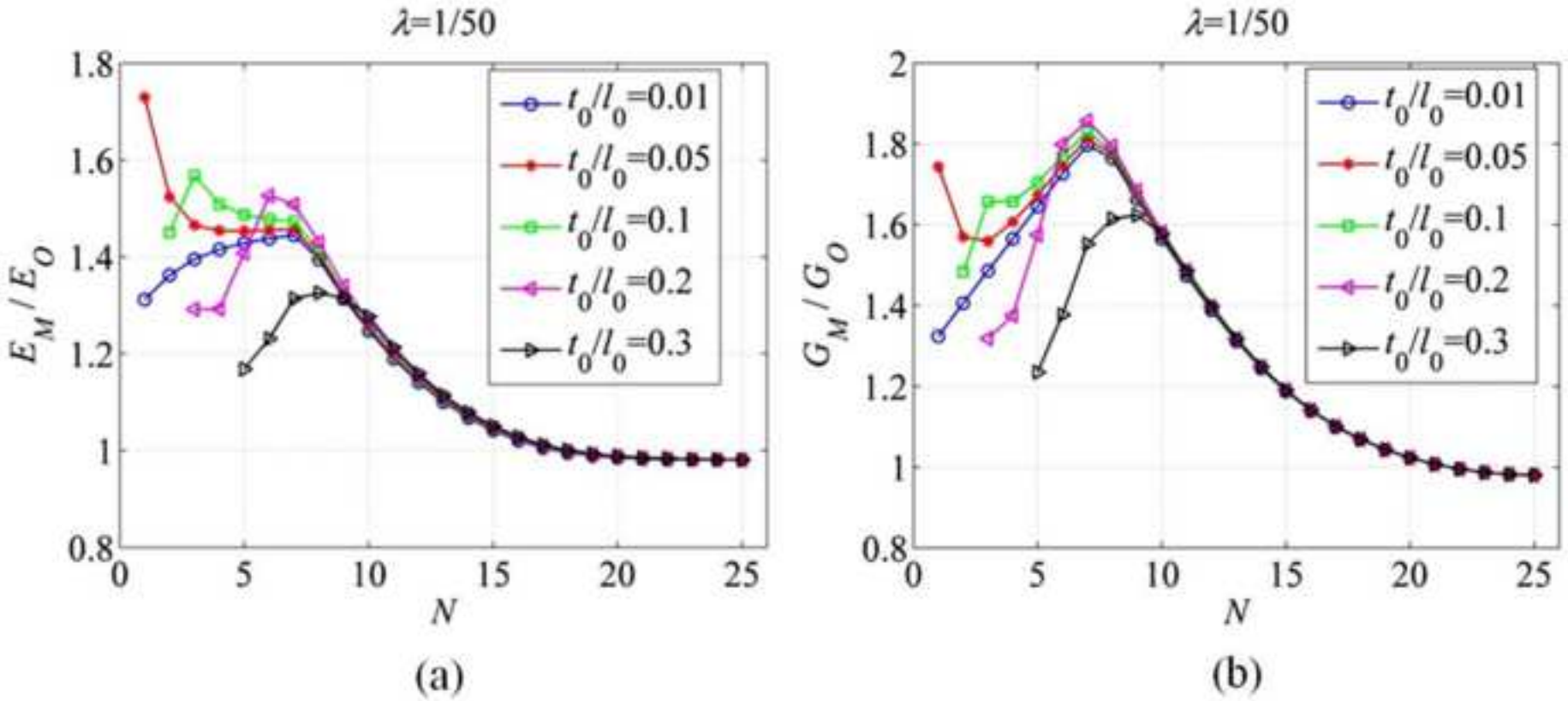

Figure 5

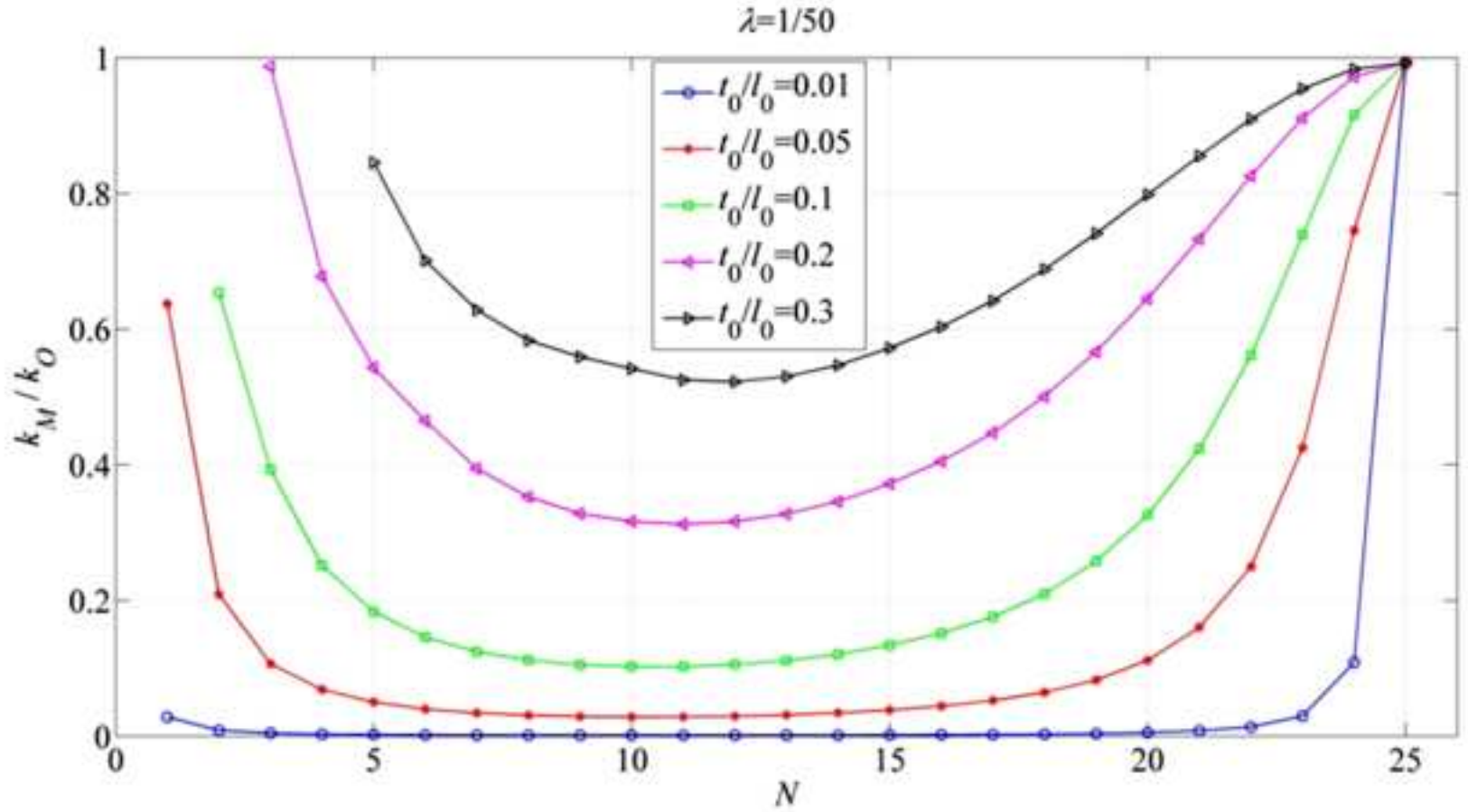

Figure 6

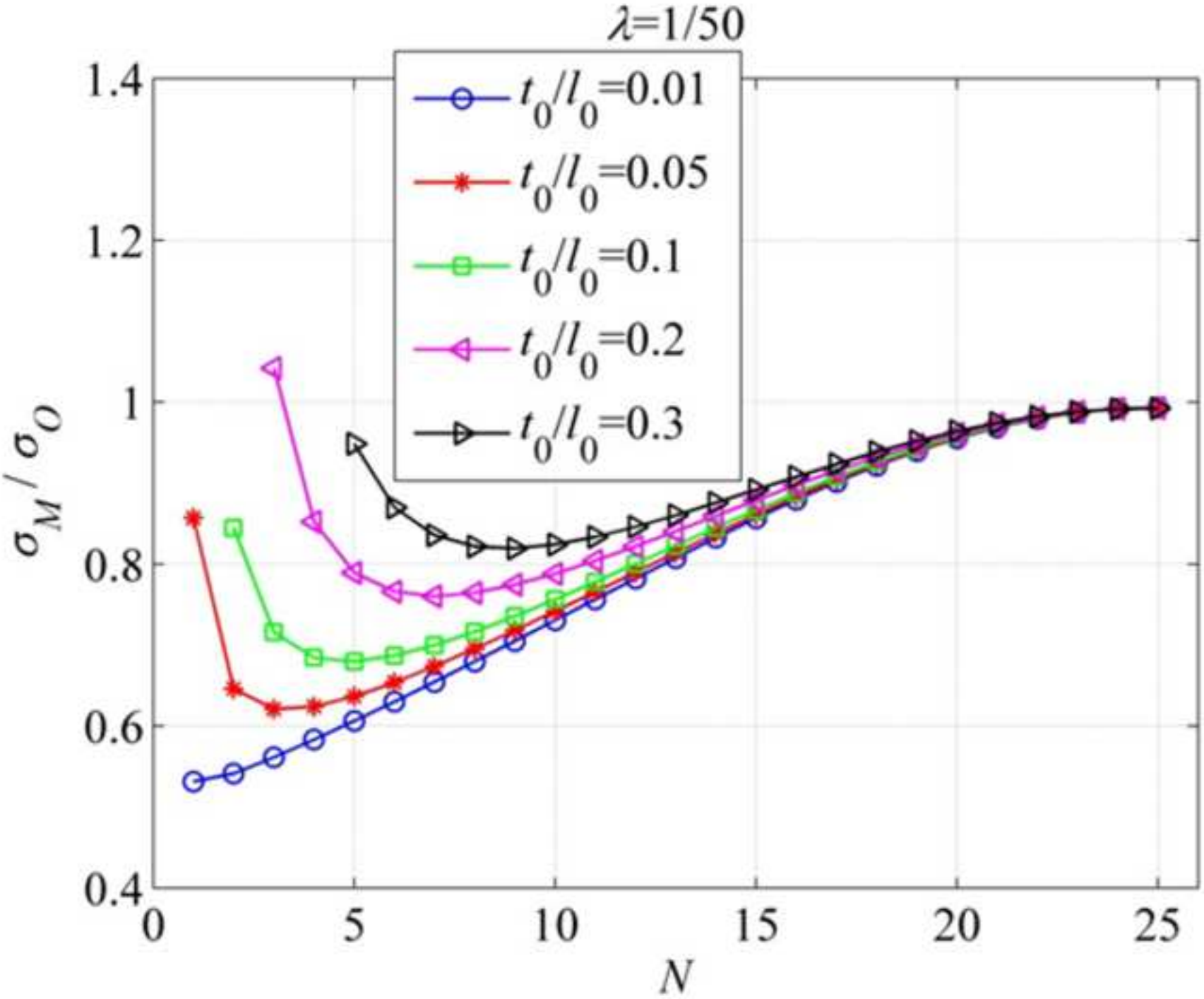

Figure 7

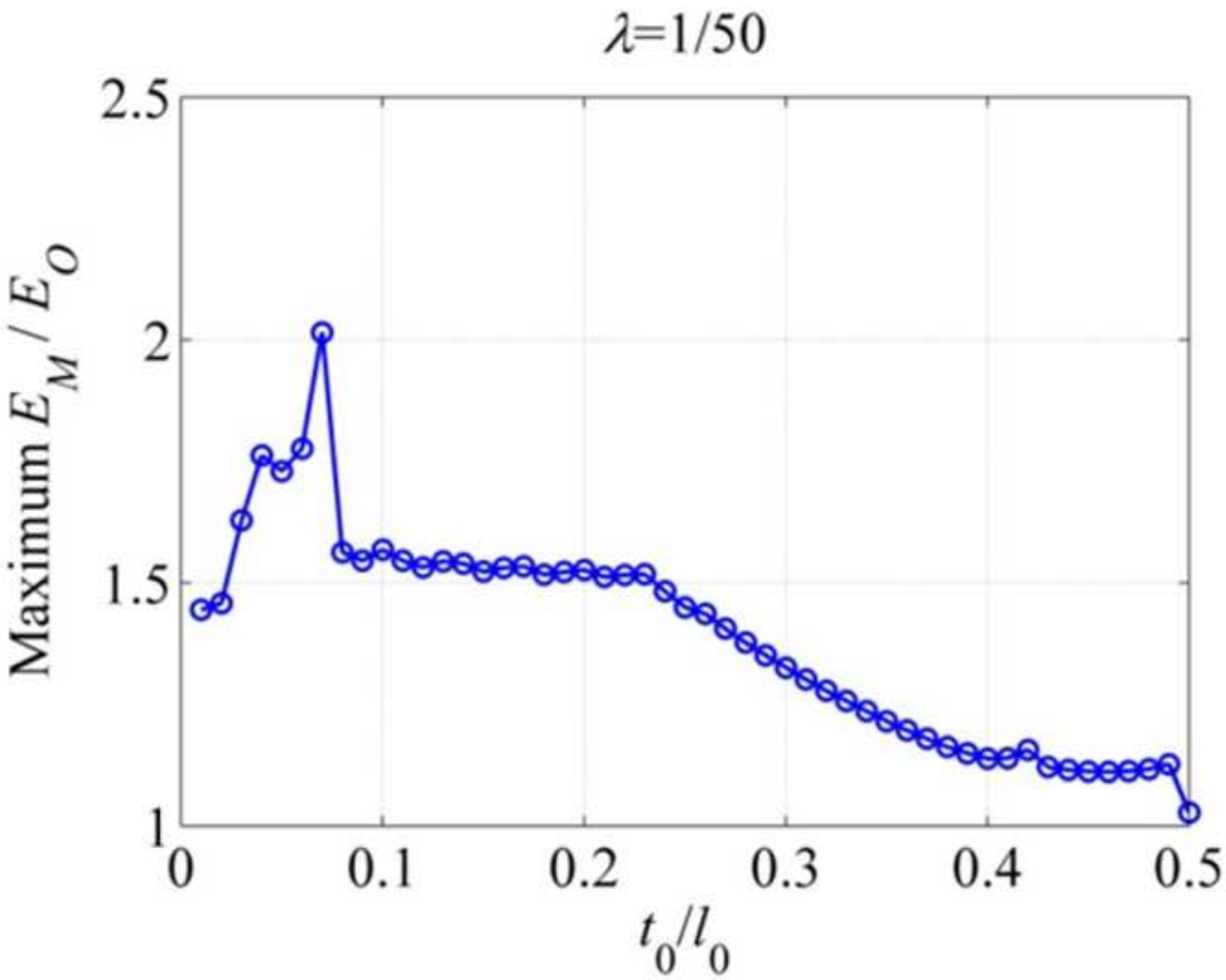

Figure 8

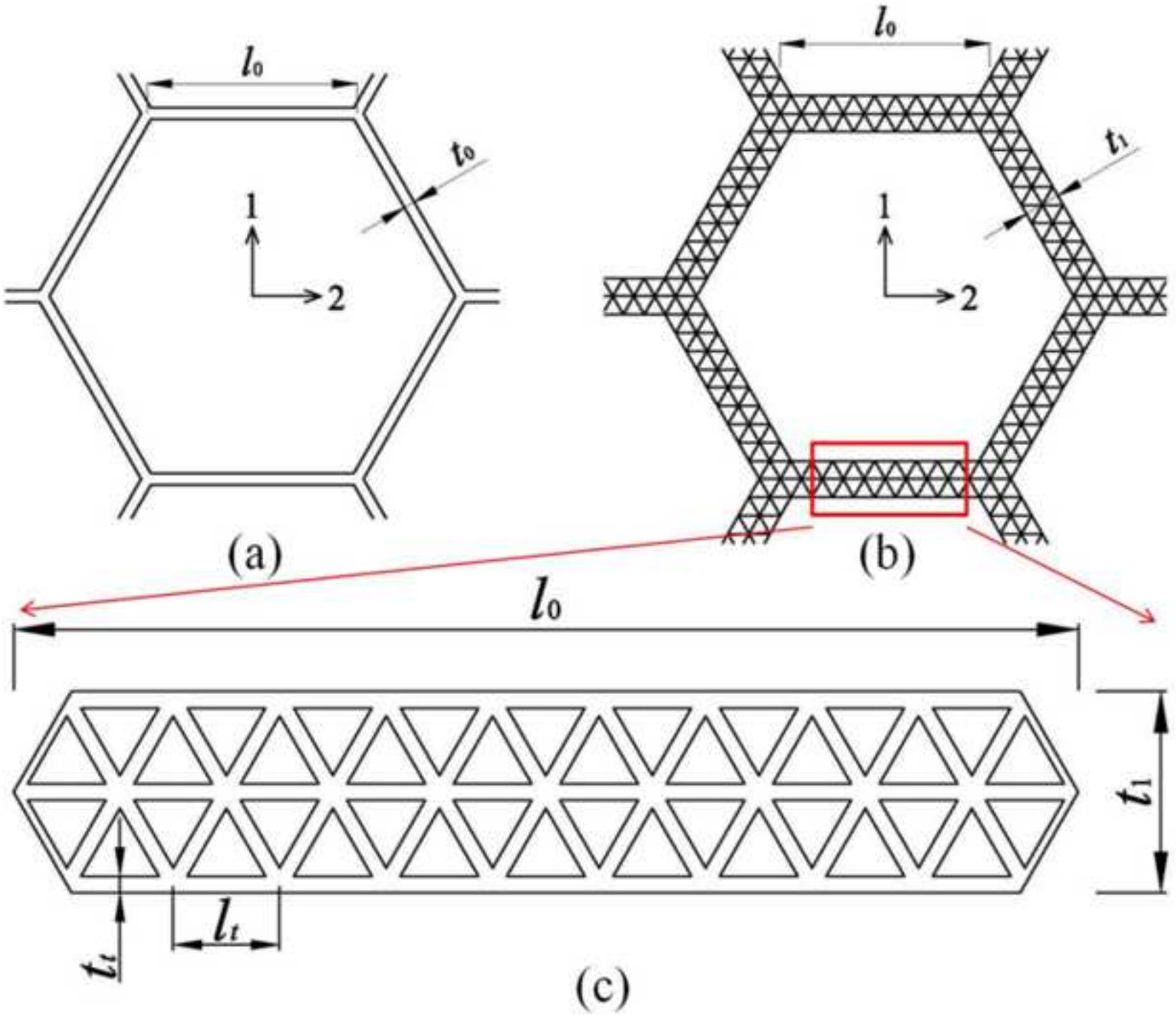

Figure 9

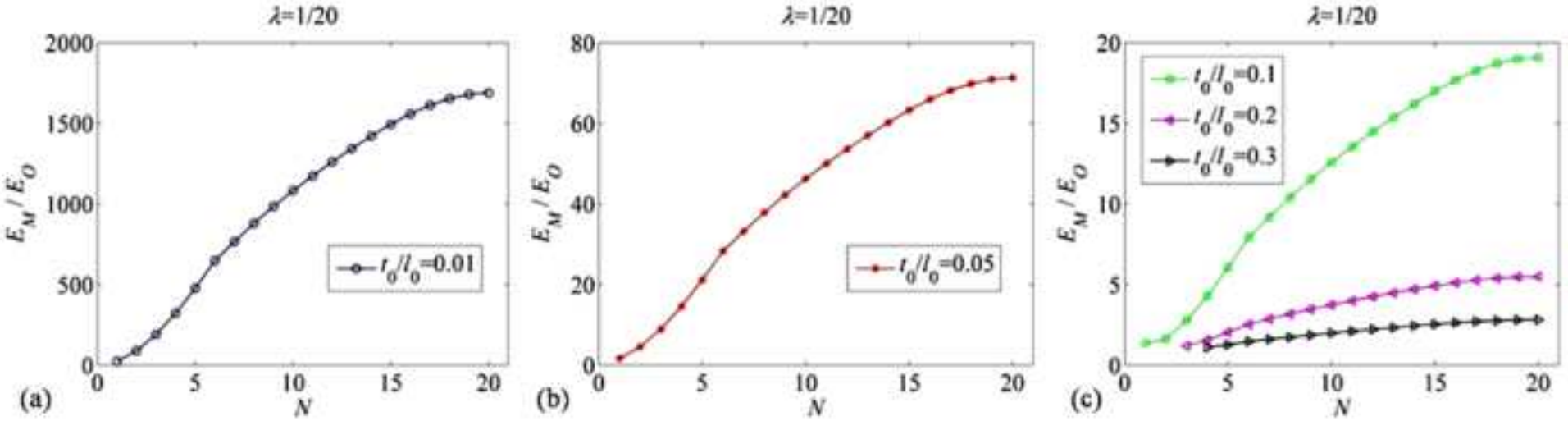

Figure 10

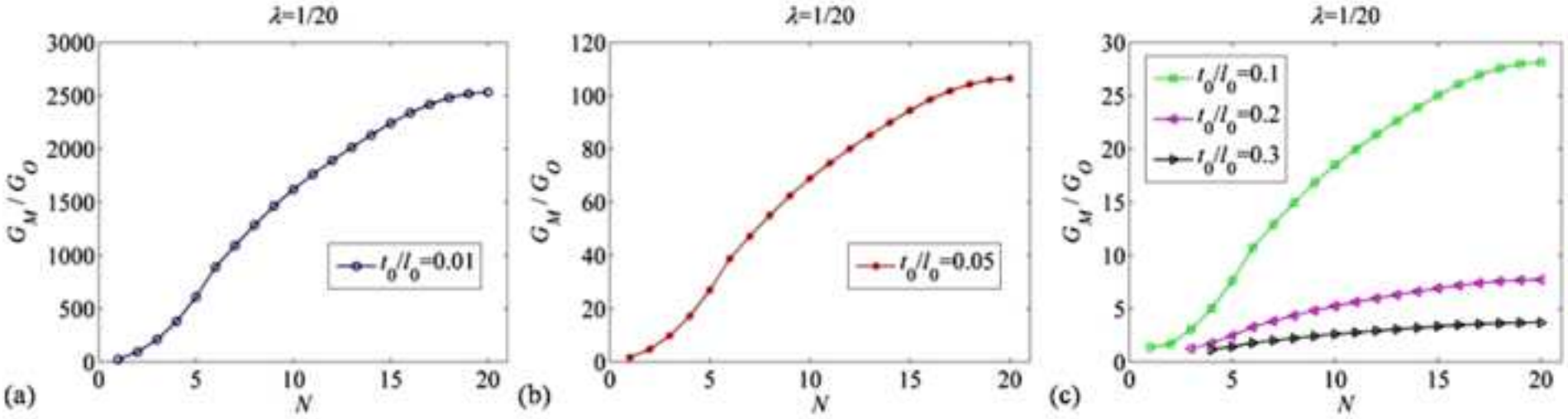

Figure 11

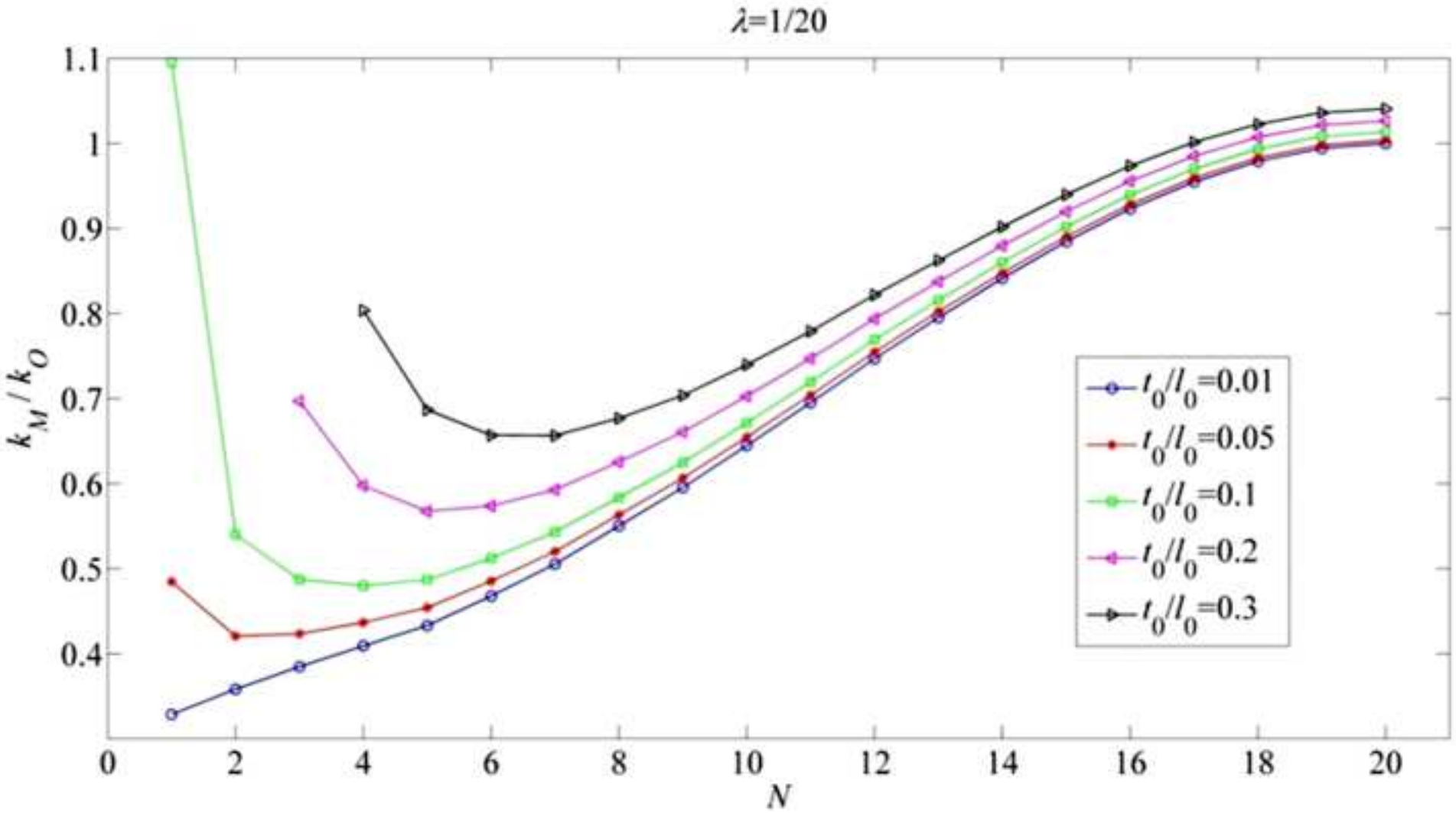

Figure 12

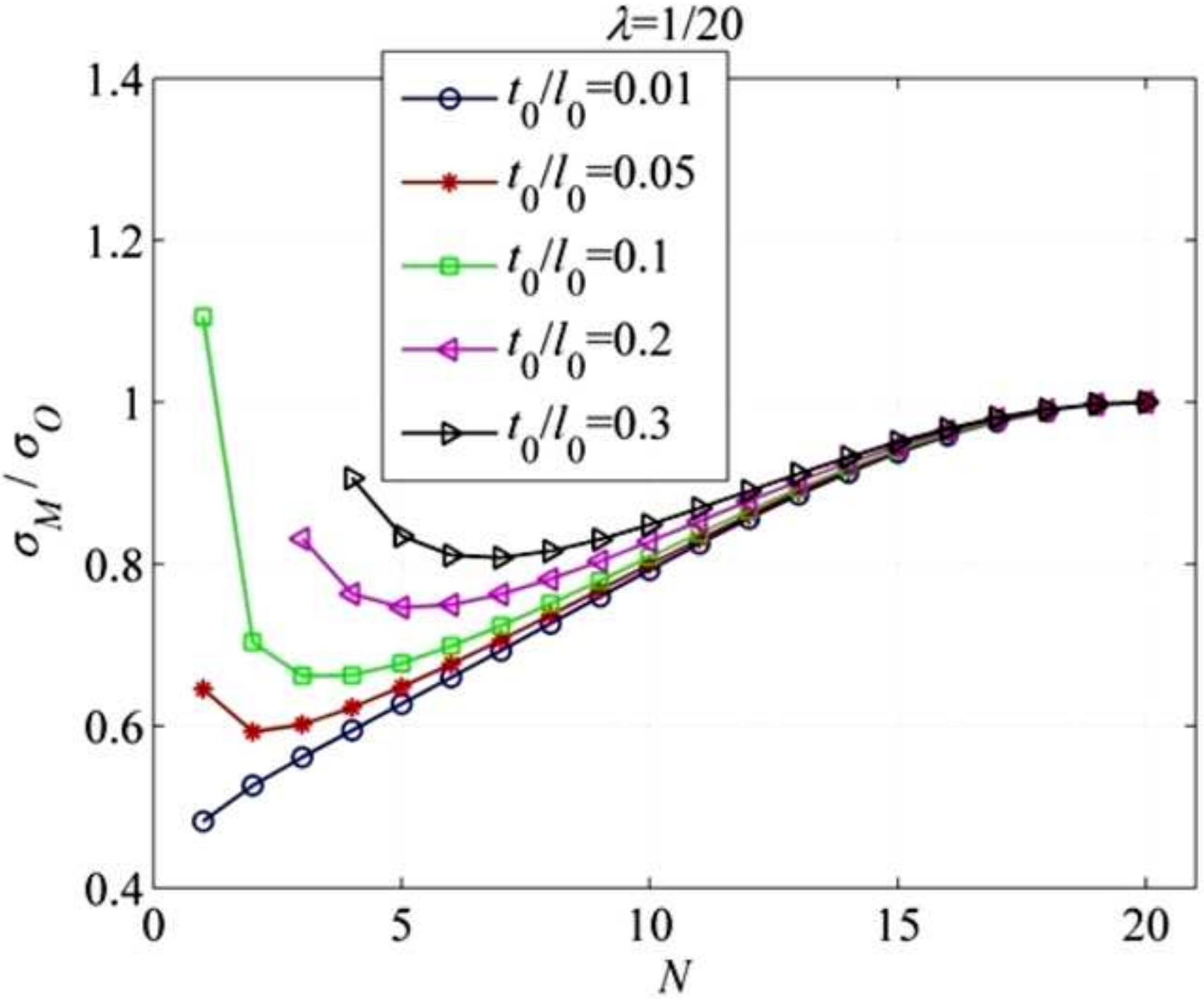

Figure 13

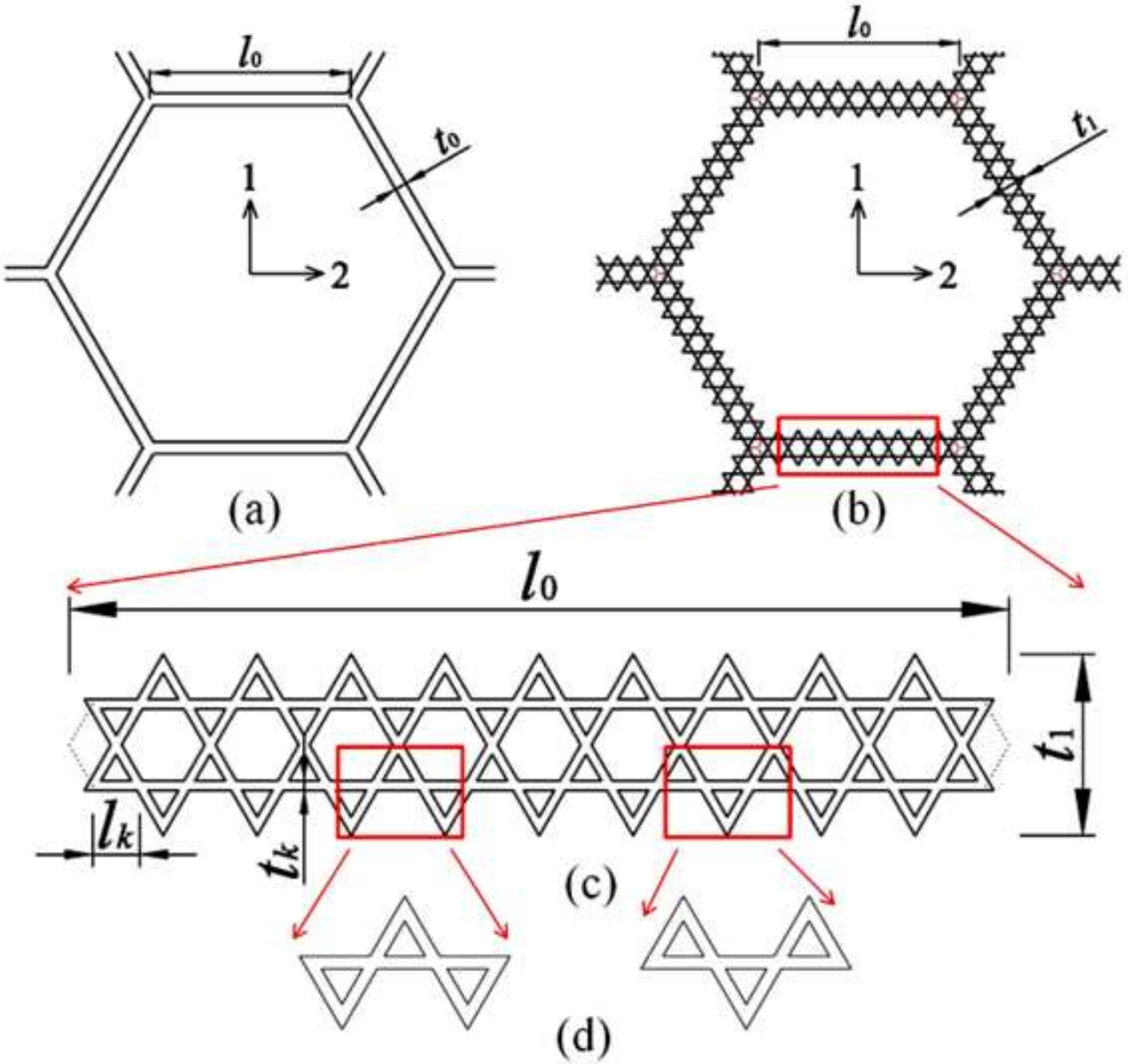

Figure 14

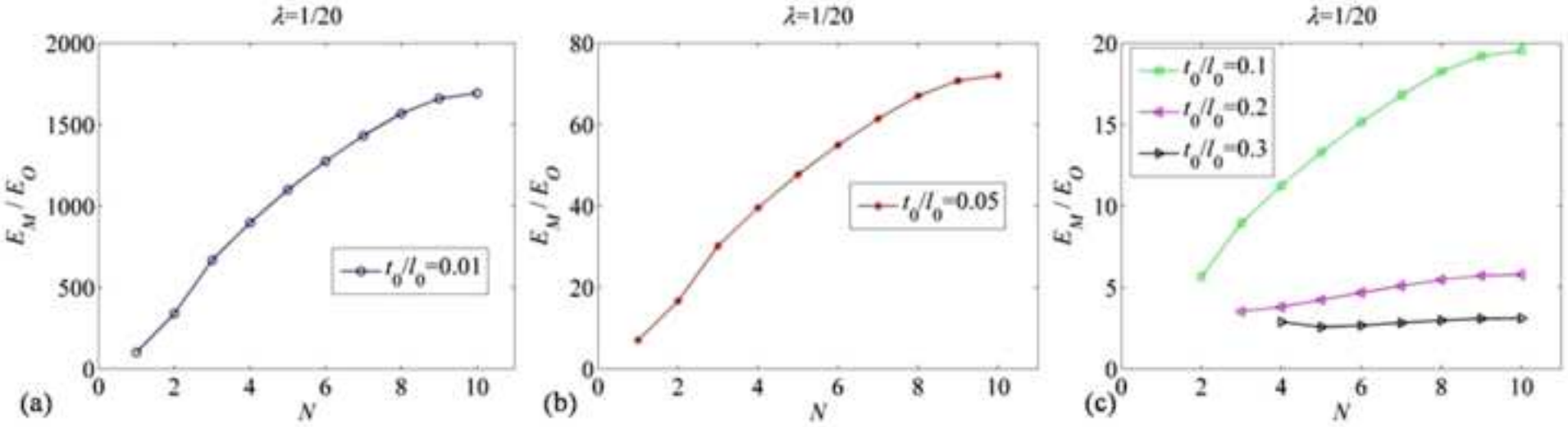

Figure 15

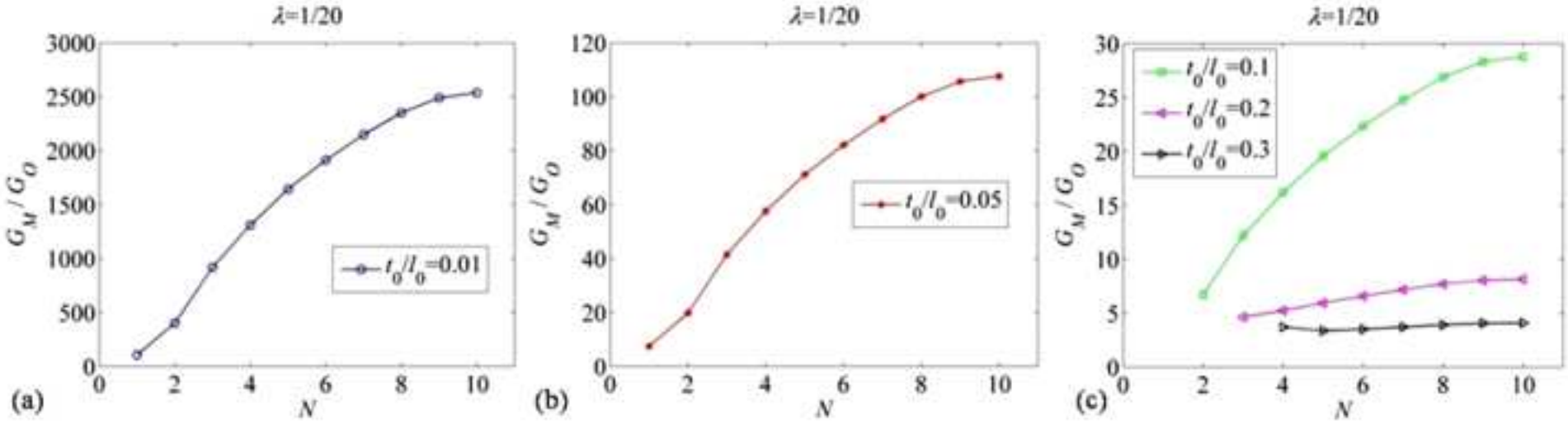

Figure 16

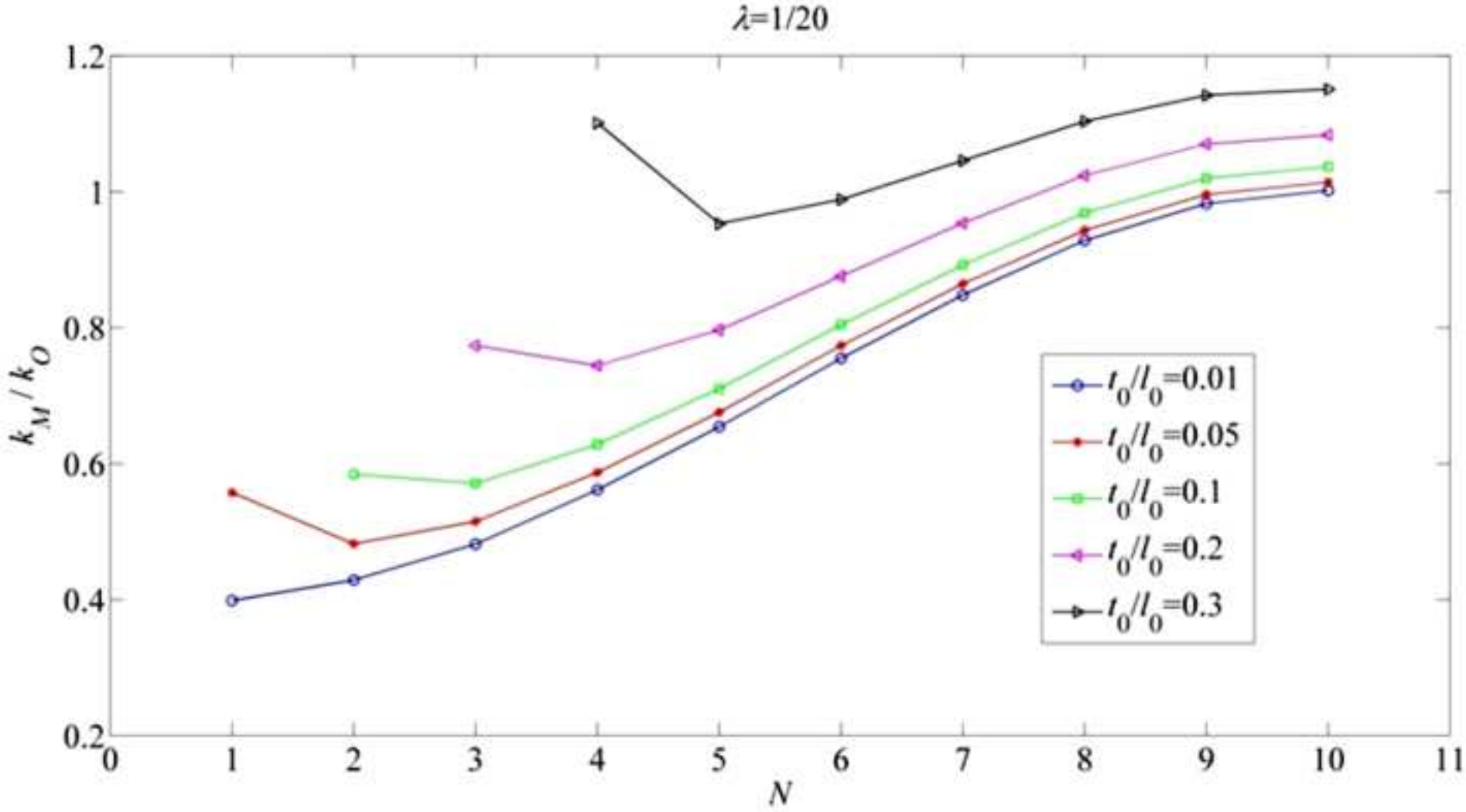

Figure 17

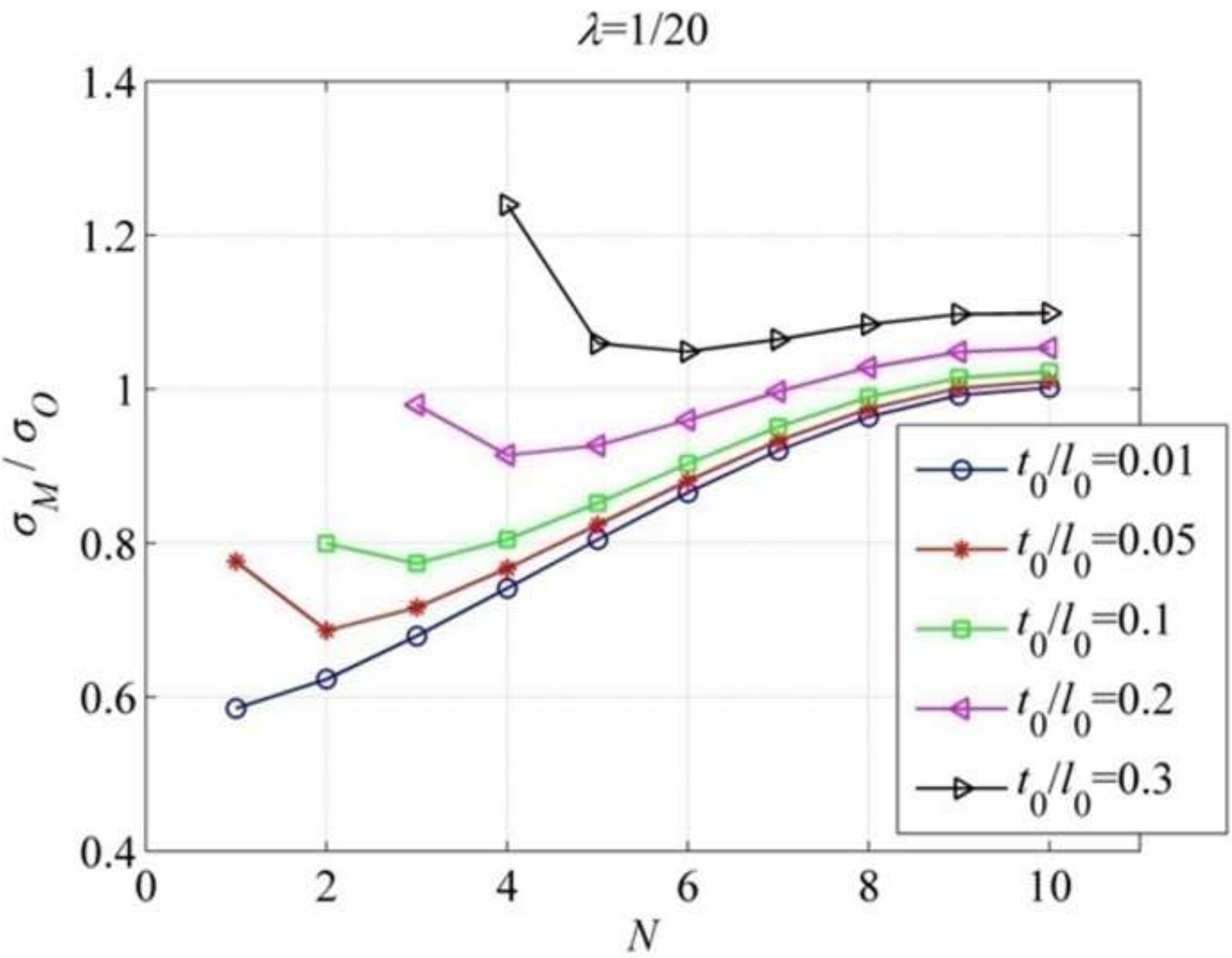

Figure 18

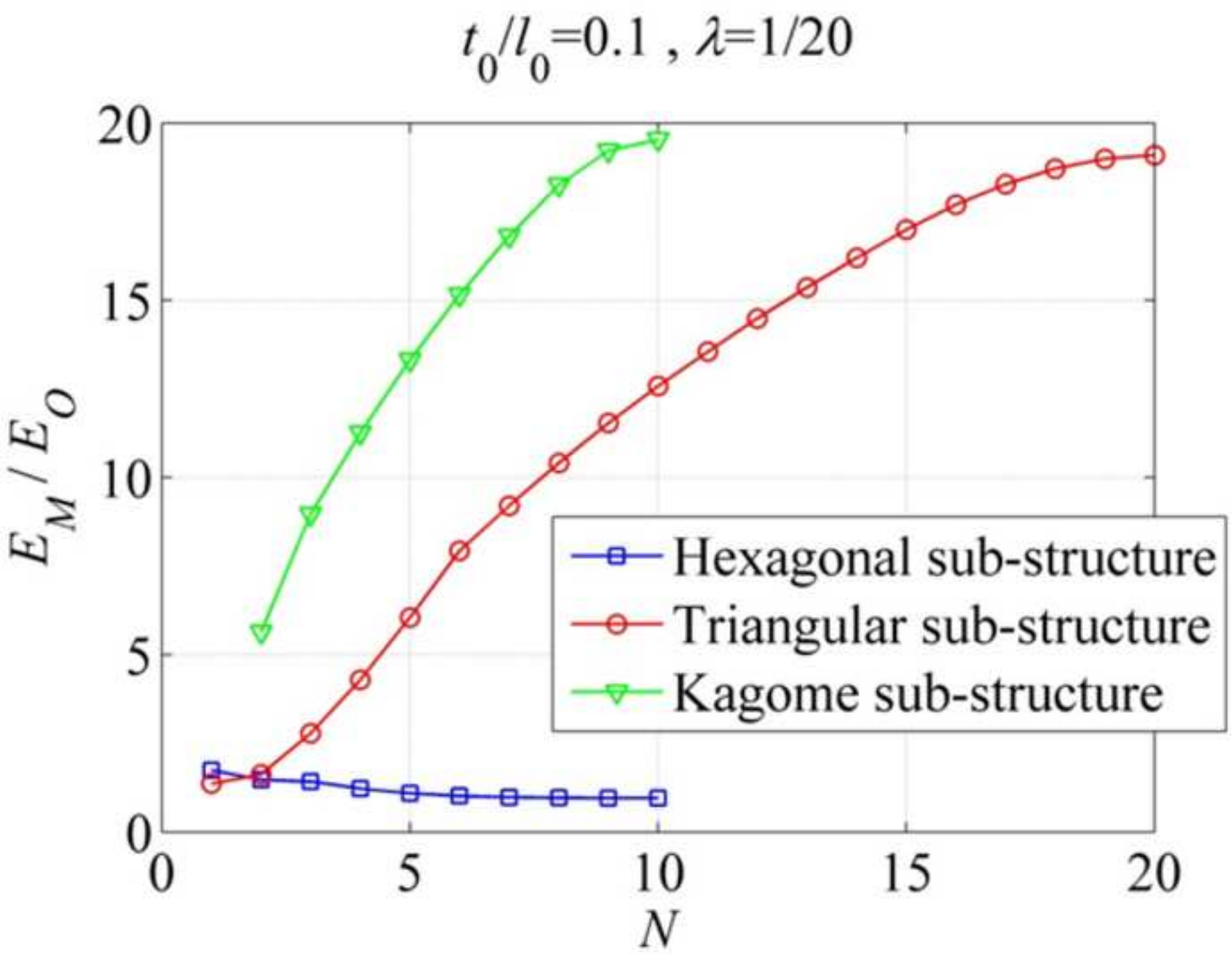

Figure 19

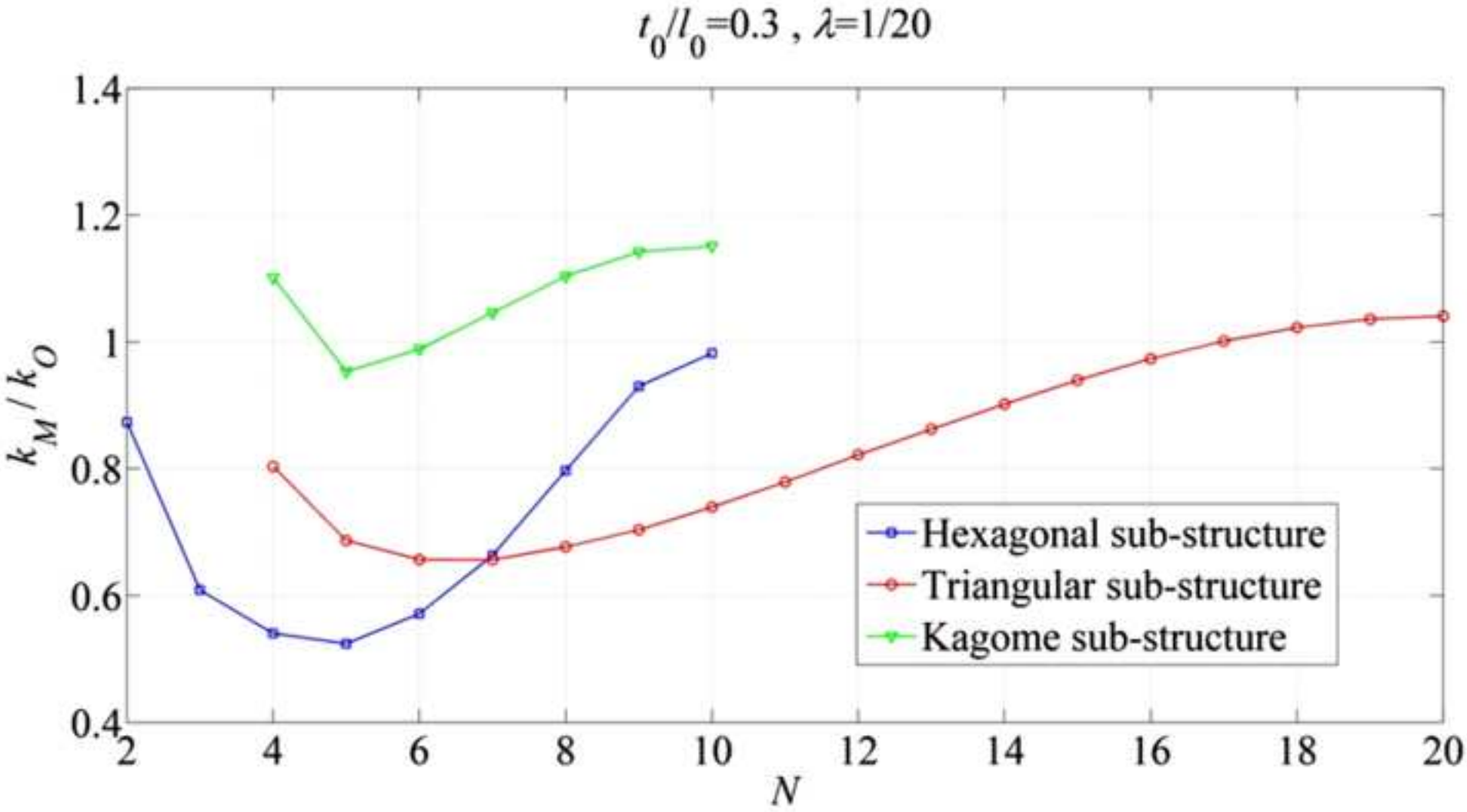

Figure 20

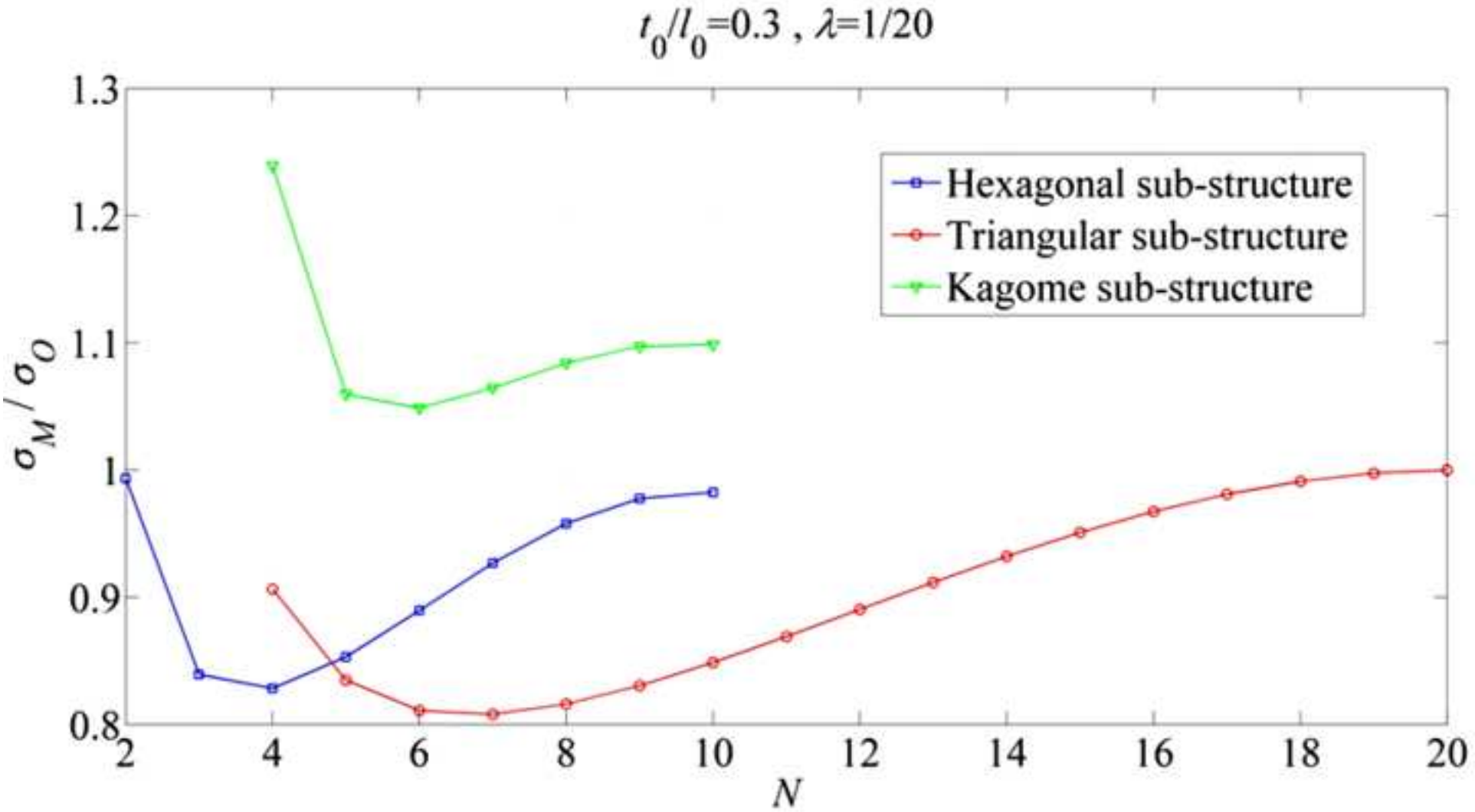

Figure A.1

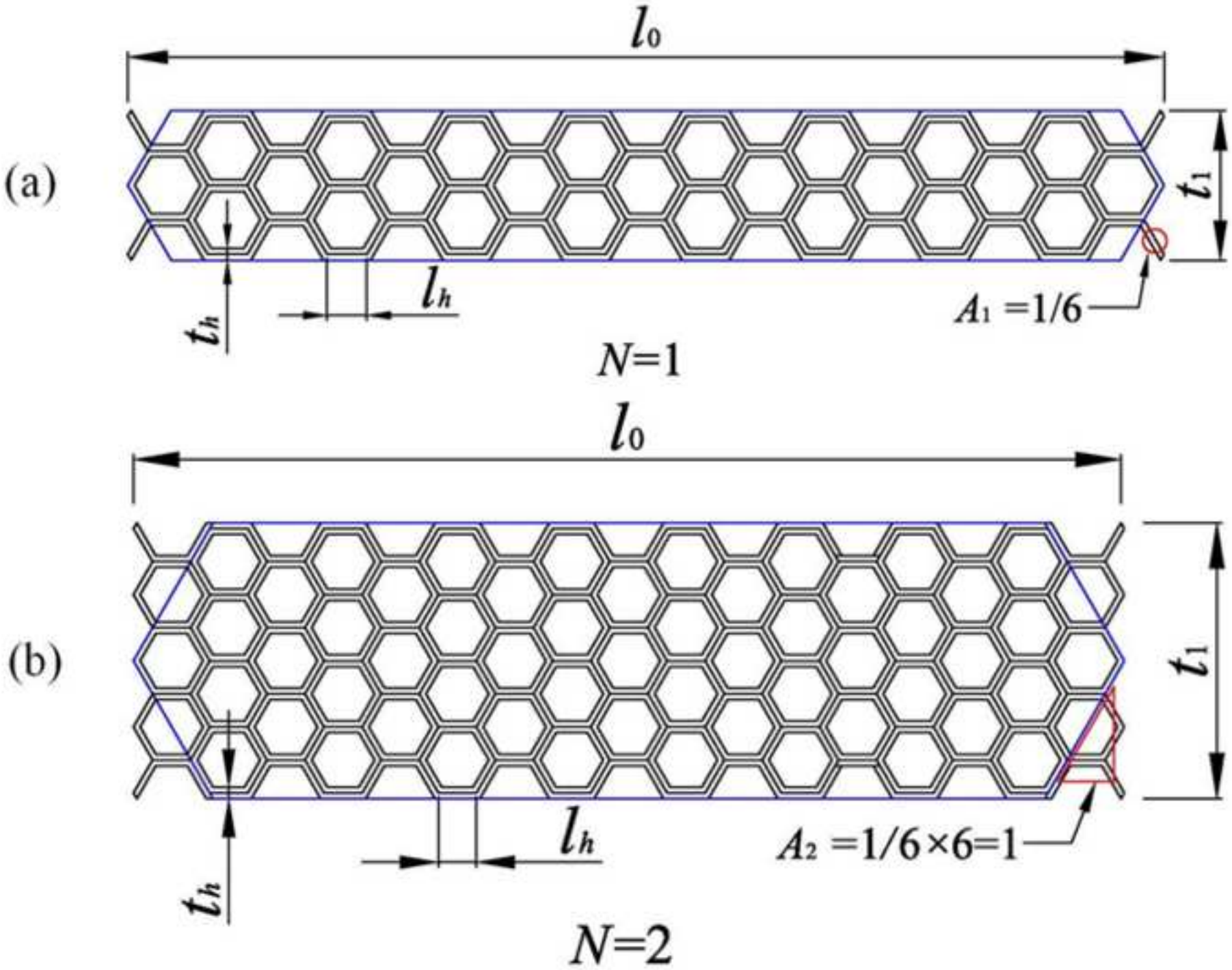

Figure B.1

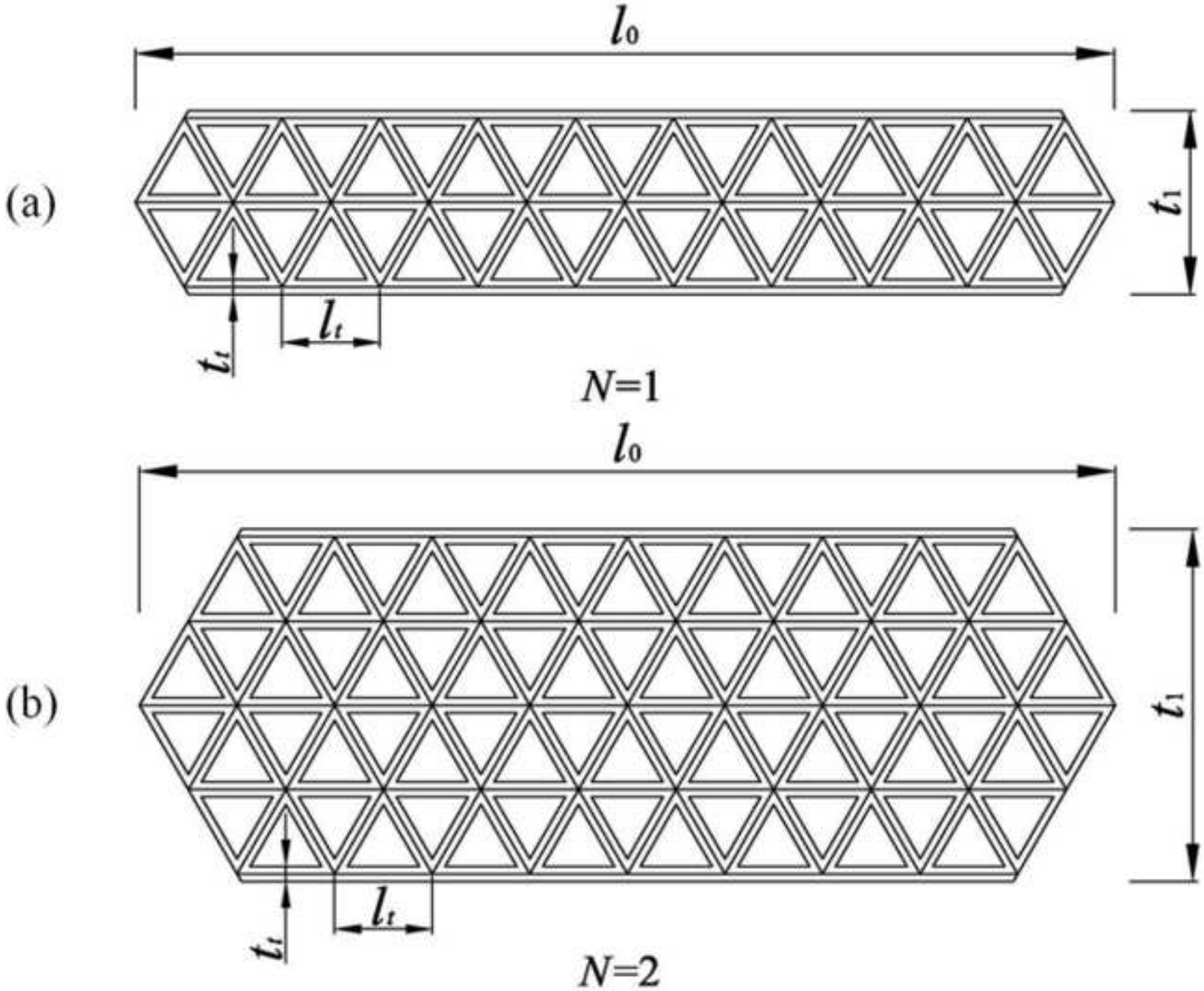

Figure C.1